https://doi.org/10.5194/egusphere-2025-1831
Preprint. Discussion started: 3 June 2025

SWIIFT v0.10: a numerical model of wave-induced sea ice breakup based on an energy criterion

Nicolas Guillaume Alexandre Mokus[1], Véronique Dansereau[1,2], Guillaume Boutin[3], Jean-Pierre Auclair[1,4], and Alexandre Tlili[1,5]

[1]Univ. Grenoble Alpes, Univ. Savoie Mont Blanc, CNRS, IRD, Grenoble INP, ISTerre, 38000 Grenoble, France
[2]Univ. Grenoble Alpes, CNRS, IRD, Grenoble INP, IGE, 38000 Grenoble, France
[3]Nansen Environmental and Remote Sensing Center, Bergen, Norway
[4]Now at Department of Chemical and Environmental Engineering, Technical University of Cartagena, 30203 Cartagena, Spain
[5]Now at Université Paris–Saclay, CNRS, CEA, Service de Physique de l'État Condensé, 91191 Gif-sur-Yvette, France

Correspondence: Nicolas Guillaume Alexandre Mokus (nicolas.mokus@univ-grenoble-alpes.fr)

Abstract. The wave-induced breakup of sea ice contributes to the formation of the marginal ice zone in the polar oceans. Understanding how waves fragment the ice cover into individual ice floes is thus instrumental for accurate numerical simulations of the sea ice extent and its evolution, both for operational and climate research purposes. Yet, there is currently no consensus on the appropriate fracturing criterion, which should constitute the starting point of a physically sound wave–ice model. While fracture by waves is commonly treated within a hydroelastic framework and parameterised with a maximum strain-based criterion, in this study we explore a different, energy-based, approach to fracturing. We introduce SWIIFT (Surface Wave Impact on sea Ice—Fracture Toolkit), a one-dimensional model, based on linear plate theory, into which we incorporate this energy fracture criterion. We demonstrate it with simple simulations that reproduce existing laboratory wave-induced breaking experiments of an analogue material, allowing qualitative comparisons. We find that under some wave conditions, identified by a dimensionless wavenumber, corresponding to in situ or laboratory wave-induced fracture, the model does not predict fracture at constant curvature, thereby calling into question a maximum strain criterion.

1 Introduction

In the Arctic, the newly available open ocean areas (Raphael et al., 2025) have exposed the sea ice to the effects of stronger and more frequent wave events (Thomson and Rogers, 2014). The remaining sea ice is also overall younger, thinner, more fragile and therefore more likely to be fragmented by wind, ocean currents and waves (Stroeve et al., 2012; Stroeve and Notz, 2018). In unconsolidated or fragmented ice, waves are less attenuated (Collins et al., 2015; Ardhuin et al., 2020) and can therefore propagate further into the consolidated part of the ice cover, the ice pack, and break it to a greater extent, thus enabling a wave–ice positive feedback loop (Thomson, 2022; Horvat, 2022).

This wave-induced breakup results in an assembly of floes with sizes ranging from a few metres to hundreds of metres, defining what is generally referred to as the marginal ice zone (MIZ; see Dumont, 2022, and many others). Fragmented sea ice behaves very differently from the consolidated ice pack. It is more mobile (Auclair et al., 2022) and more sensitive to

https://doi.org/10.5194/egusphere-2025-1831
Preprint. Discussion started: 3 June 2025

melt (Thomson, 2022). As a result, the MIZ response to storms can result in quick and large sea ice losses (Smith et al., 2018; Blanchard-Wrigglesworth et al., 2022), which could amplify the observed sea ice decline (Asplin et al., 2012; Thomson and Rogers, 2014). Concomitantly, high-frequency sea ice extent variability is missing in state-of-the-art climate models (Blanchard-Wrigglesworth et al., 2021), in which sea ice fragmentation by waves is not accounted for. This suggests an improved representation of the MIZ is essential to deliver accurate predictions of the sea ice evolution, over both short-term and climate time scales. However, it remains challenging as the physical processes controlling sea ice breakup are still largely unascertained, or rest on hypotheses that are not fully backed up by observations.

The first step in this development should be the identification of a fracture criterion, allowing to determine under which wave forcing (amplitude, wavelength, spectral distribution) and ice conditions (thickness, mechanical stiffness) the ice will break. To our knowledge, there is actually neither complete physical evidence nor clear consensus within the sea ice community on this criterion. To our knowledge again, all the current wave breakup modelling approaches are based on local flexural stress or strain reaching a prescribed critical value, or threshold. Behind this viewpoint is the consideration that maximum deformation will either occur at the crests and troughs of waves (for example, Dumont et al., 2011) or at the wave front (Tkacheva, 2001). These thresholds are however susceptible to be exceeded over large spans of the modelled floes, which makes super-parameterisations necessary. The location of maximum strain or stress is often considered for the fracture location (Dumont et al., 2011; Williams et al., 2017; Montiel and Squire, 2017; Mokus and Montiel, 2022), but other methods, such as computing the strain between successive wave crests and troughs only (Horvat and Tziperman, 2015) have been used.

These threshold-based criteria are consistent with (and usually come hand in hand with) an hydroelastic representation of the wave–ice system, on which a large fraction of the modelling research on wave–ice interaction lies (Squire, 2020). Wave-induced sea ice fracture has thus naturally be considered through this lens (for example, Fox and Squire, 1991; Montiel and Squire, 2017; Zhang and Zhao, 2021; Mokus and Montiel, 2022); even though more novel and computationally involved approaches exist (Herman, 2017; He et al., 2022). In the hydroelastic framework, the ice is assimilated to an elastic plate that is thin enough for the variations in the buoyancy forces acting on it to be negligible, and that therefore conforms exactly to the shape of the ice–ocean interface. When associated with a critical strain fracturing criterion, this framework has shown some agreement with observations (Kohout et al., 2016; Voermans et al., 2020). It has also allowed wave and floe-resolving numerical simulations to generate floe size distributions (Kohout and Meylan, 2008; Ren et al., 2021; Mokus and Montiel, 2022), and has therefore percolated into coupled global sea ice models (Roach et al., 2019; Bateson et al., 2020; Yang et al., 2024).

The current contribution digs into the question of the fracturing criterion for the fragmentation of sea ice by waves. In this, we are motivated by recent laboratory results investigating the response of an analogue material to wave forcing (Auvity et al., 2025). In particular, these authors highlighted that the curvature at which their material broke is not constant, but depends monotonically on the applied wavelength. The spread in reported sea ice critical strains (Kohout and Meylan, 2008) could thus be an artefact hiding such a relationship. In this context, we investigate an approach based on a model of fracture propagation in elastic solids (Griffith, 1921) which is common in the field of fracture mechanics. It opposes the energetic cost of creating new surfaces to the elastic energy stored in a material. The resulting energy-based fracture criterion includes the effect of bending deformation as it depends on the associated elastic deformation energy, but is non-local as it is integrated over the length of

https://doi.org/10.5194/egusphere-2025-1831
Preprint. Discussion started: 3 June 2025

the deformed ice floe. It leads to a unique solution. Since the original work of Griffith (1921), this model has been updated (Francfort and Marigo, 1998; Francfort, 2021) and built upon specifically for application to sea ice (Mulmule and Dempsey, 1997; Balasoiu, 2020). Measurements of sea ice fracture toughness, which can be linked to the energetic cost of fracturing, have been compiled by Dempsey (1991) and an extensive body of work also exists on freshwater ice (for example, Gharamti et al., 2021a, b).

With the intent on focusing on the deformation and resulting fracturing of the ice, we have implemented this energy-based criterion in a framework that differs from the hydroelastic representation in that the ice is not assumed to conform to the water surface, but freely deforms within the wave field as a result of the local buoyancy and gravity forces. The resulting simple, yet versatile, 1D model also accommodates a strain-based fracture criterion. It thereby allows investigating the effect of using either criterion on the occurrence of the fracture and, eventually, on the extent of a simulated MIZ, and shape of the associated floe size distribution. Another use case of this model is the comparison to laboratory experiments on fracture, conducted on sea ice or analogue materials, which we pursue in this study.

The paper is divided as follows: in Sect. 2, we give a general mathematical description of the model, including the treatment of sea ice as an elastic plate, the formulation of the breakup criteria, and the representation of waves. In Sect. 3, we give specific information pertaining to the numerical results we present in Sect. 4, that is, the particular setup of the model in this study. We discuss these results in Sect. 5.

2 Floe and fracture model

A common assumption behind wave–elastic plate interaction models (for example, Fox and Squire, 1991; Tkacheva, 2001; Mokus and Montiel, 2022) is to consider the plate thin enough for variations of the buoyancy force acting on it to be negligible. The plate is, however, subjected to the fluid pressure acting on its bottom side, and it is assumed that the plate conforms to the fluid motion at all times. Fluid pressure is determined by solving for the fluid flow, typically by assuming a potential flow. To develop the model presented herein, we adopt a different approach, motivated by our interest in the ice deformation and fracture, whereas the focus of fluid-centred models has historically been that of wave scattering and attenuation by the plate.

In this study, the ice cover is considered thick enough for the local changes in buoyancy force to not be negligible. We do not explicitly resolve the fluid flow underneath the plate, and impose no condition on the ice–ocean interface. Instead, we solve for the vertical deflection of the ice stemming from the local balance of gravity and buoyancy forces driven by the sea surface displacement. The fluid surface thus acts as a forcing term, which is made aware of the presence of the ice floes only through parameterised attenuation. A consequence is that floes can locally be immersed. In fact, our model interpolates between the limits of an elastic floe that conforms perfectly to the wave surface, and of a rigid floe only capable of solid motion, which can therefore be submerged. We quantify this behaviour with the dimensionless wavenumber kL_D, that relates the wavenumber of the forcing wave k (formally introduced in Sect. 2.3.1) to the flexural length of the floe L_D (formally introduced in Sect. 3.1). The small kL_D limit (long wave, compliant floe) corresponds to the strain formulation of Dumont et al. (2011), while the large kL_D limit (short wave, rigid floe) corresponds to their stress formulation.

https://doi.org/10.5194/egusphere-2025-1831
Preprint. Discussion started: 3 June 2025

We do not consider the reflection of waves at the ice–water interface (for example, Mokus and Montiel, 2022) nor the compression due to wave radiation (for example, Herman, 2018) or any surge motion, and take note that the model would be more complete if the pressure forcing associated with the contact between the ice and the water was explicitly taken into account.

2.1 Governing mechanical equations

Our one-dimensional model considers a fluid volume of finite or infinite depth, equipped with a Cartesian coordinate system (x, z) where z is the vertical coordinate oriented upward, as shown in Fig. 1. We assume translational invariance in the second horizontal direction. The domain is populated with floating ice floes of prescribed positions and lengths, which may not overlap. Any part of the domain not covered with ice is deemed to be open water.

As in the work of Meylan et al. (2015), the deformation of the ice cover is derived using the Kirchhoff–Love thin-plate theory. The ice is thus considered homogeneous, isotropic, and transversally loaded by body forces. We assume a constant thickness h along a given floe, although different floes can have different thicknesses. The two forces acting on the ice are buoyancy and gravity. In the case of a fluid at rest (no waves), equating the gravity force per unit area and the buoyancy force per unit area allows expressing the draught of a floe, d, as

$$\rho_i h \boldsymbol{g} - \rho_w d \boldsymbol{g} = 0 \Leftrightarrow d = \frac{\rho_i}{\rho_w} h, \tag{1}$$

where ρ_i is the density of the ice, ρ_w the density of the ocean water and $\boldsymbol{g}$ the gravitational field.

We now move away from this rest state, and impose a perturbation of the fluid surface $\eta(x)$. Because the propagation speed of elastic waves in sea ice is several orders of magnitude greater than that of surface gravity waves (Moreau et al., 2020a), we consider this perturbation and the resulting floe deformation to be quasi-static. Thus, we only consider one independent variable, the space coordinate x, and no explicit time dependency. The vertical displacement $w(x)$ corresponding to this perturbed state is determined by the local balance between gravity and buoyancy. The weight per unit area of the ice is still $\rho_i h \boldsymbol{g}$. However, the height of displaced fluid now corresponds to the difference between the fluid surface $\eta(x)$ and the displaced bottom of the ice floe, $w(x) - d$. Locally, the buoyancy force per unit area is thus $-\rho_i \big[\eta(x) - \big(w(x) - d\big)\big]\boldsymbol{g}$; this is illustrated in Fig. 1. The floe is then subjected to the resulting body force

$$\boldsymbol{q}(x) = \rho_i h \boldsymbol{g} - \rho_w \big[\eta(x) - \big(w(x) - d\big)\big]\boldsymbol{g} \tag{2}$$

$$= -\rho_w [\eta(x) - w(x)]\boldsymbol{g}, \tag{3}$$

and projecting $\boldsymbol{q}$ onto the vertical axis gives

$$q(x) = \rho_w g [\eta(x) - w(x)]. \tag{4}$$

Using the bending equation of a loaded plate, we then obtain a differential equation on the deflection of the floe,

$$D \frac{\mathrm{d}^4 w}{\mathrm{d}x^4} = \rho_w g \big[\eta(x) - w(x)\big], \tag{5}$$

https://doi.org/10.5194/egusphere-2025-1831
Preprint. Discussion started: 3 June 2025

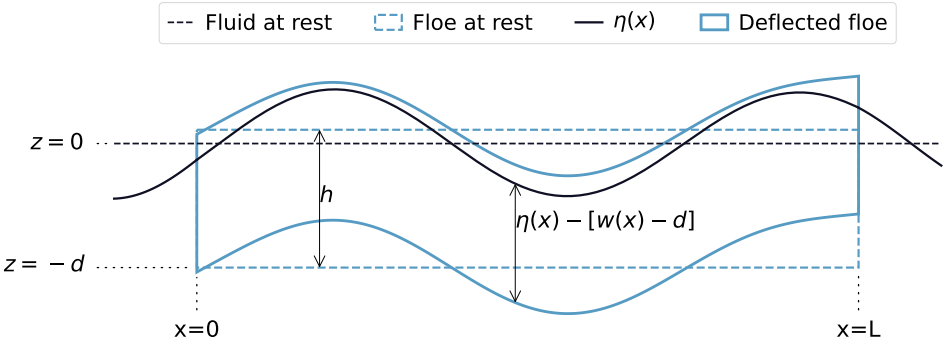

Figure 1. Schematic of a deformed ice floe in a wave field. The horizontal dashed line represents the sea surface at rest in the absence of ice, which we use as the reference level. The dashed rectangle represents a floe at rest. A perturbation of the fluid surface (solid line) in the free-surface regions imposes a deflection of the ice floe (solid-lined shape). This corresponds to a model output, with ice thickness $50\,\mathrm{cm}$, floe length $120\,\mathrm{m}$, forcing wave with amplitude $20\,\mathrm{cm}$ and wavelengths $76.4\,\mathrm{m}$ (open water) and $84.3\,\mathrm{m}$ (ice-covered water).

where we take advantage of the simplifying hypotheses made on our geometry. We introduced the flexural rigidity $D = \frac{Yh^3}{12(1-\nu^2)}$, characterising the ability of the plate to resist bending, with Y and ν the Young's modulus and Poisson's ratio of the plate. We complete Eq. (5) with free-edge boundary conditions, that is, vanishing moment and force at both ends of the ice floe of length L. We choose a reference frame local to the floe, where $x = 0$ corresponds to its left edge, so that the complete boundary problem can be written

$$\begin{cases} \dfrac{\mathrm{d}^4 w}{\mathrm{d}x^4} = \left(\dfrac{D}{\rho_w g}\right)^{-1} \left[\eta(x) - w(x)\right] & x \in [0, L] \quad \text{(6a)} \\ \dfrac{\mathrm{d}^2 w}{\mathrm{d}x^2} = 0 & x \in \{0, L\} \quad \text{(6b)} \\ \dfrac{\mathrm{d}^3 w}{\mathrm{d}x^3} = 0 & x \in \{0, L\}. \quad \text{(6c)} \end{cases}$$

For prescribed wave conditions and material properties, solving Eq. (6) thus provides the deflection w of the floe.

2.2 Fracture

2.2.1 Energy criterion

Unlike the prevalent maximum strain formalism commonly used by the sea ice community when modelling wave–ice interactions (for example, Kohout and Meylan, 2008; Dumont et al., 2011; Horvat and Tziperman, 2015; Ren et al., 2021), we develop a breakup criterion from the framework of fracture mechanics, based on the consideration that in brittle, elastic materials, fracture happens to minimise the internal energy associated with deformation (Griffith, 1921). In this framework, the total energy to be minimised is the sum of the elastic energy E_{el} associated with the deformation (in our case, bending) of the material, and

https://doi.org/10.5194/egusphere-2025-1831
Preprint. Discussion started: 3 June 2025

of the fracture energy E_{fr} associated with the creation of new surfaces around a crack. This energy decomposition is consistent with mode I fracturing, which in the case of our model translates to vertical fractures due to in-plane tensile stress.

The linear (in the x-direction) elastic energy density (per unit length in the second horizontal direction, and per unit thickness) in a homogeneous, unstretchable and linear elastic material is

$$W_{\mathrm{el}} = \frac{D}{2h}\kappa^2(x) \tag{7}$$

with

$$\kappa(x) = \frac{\mathrm{d}^2 w}{\mathrm{d}x^2} \tag{8}$$

the local linear floe curvature due to the deformation. Equation (7) stems from integrating the density of elastic energy (per unit volume) along the axis normal to the neutral plane of the plate (in our case, the z-direction), and takes into account stretching or compression in the directions of the plane (in our case, simply the x-direction). By integrating Eq. (7) along the floe, we obtain the surface energy density,

$$E_{\mathrm{el}} = \frac{D}{2h}\int_0^L \kappa^2(x)\,\mathrm{d}x. \tag{9}$$

The fracture energy density E_{fr} relates to the energy required to create a new surface. In the case where the only admissible fractures vertically break the ice through its entire thickness, we simplify the formulation from Francfort and Marigo (1998) as

$$E_{\mathrm{fr}} = N_{\mathrm{fr}} G \tag{10}$$

with N_{fr} the number of fractures, and G the energy release rate (analogous to the surface tension for fluids). Again, note that this energy is expressed per unit surface normal to the x-direction.

To determine whether a floe breaks, we compare two energy states: that of the unbroken, deformed floe, and a hypothetical state in which this floe has fractured into several fragments. In the former state, the elastic energy, noted E^0_{el}, is that of the deformed floe, as defined in Eq. (9). In the latter state, the total elastic energy, noted E^s_{el}, is the sum of the elastic energies of the individual newly broken floes. If the broken state is—from an energy standpoint—favourable, it should replace the unbroken state. Formally, we look for the finite set of the fracture locations, $\boldsymbol{x}^{\mathbf{fr}} = \{x_j \mid x_j \in (0, L)\}$. This set has size N_{fr}, the number of cracks, dividing the original floe into $N_{\mathrm{fr}} + 1$ fragments. It should minimise the free energy F defined as

$$F(\boldsymbol{x}^{\mathbf{fr}}) = E_{\mathrm{fr}}(N_{\mathrm{fr}}) + E^s_{\mathrm{el}}(\boldsymbol{x}^{\mathbf{fr}}) - E^0_{\mathrm{el}} \tag{11}$$

with the additional constraint that for breakup to occur, we must have $F < 0$. In other words, a floe breaks if the elastic energy released by the breakup exceeds the energetic cost of the breakup. If no such set can be found, we conclude that the current deformation of the floe is not sufficient to fracture it. The post-fracture elastic energy expands to

$$E^s_{\mathrm{el}} = \frac{D}{2h}\sum_{j=0}^{N_{\mathrm{fr}}}\int_{x_j}^{x_{j+1}} {\kappa_j}^2(x)\,\mathrm{d}x \tag{12}$$

https://doi.org/10.5194/egusphere-2025-1831
Preprint. Discussion started: 3 June 2025

with $x_0 = 0$ and $x_{N_{\rm fr}+1} = L$. The curvatures κ_j are obtained from solving Eq. (6) individually for every (at this stage, still hypothetical) fragments.

Equation (11) has an explicit dependency to the number of fractures allowed to happen for a given quasi-static state, that is, at a given time. It suggests that the size of $\boldsymbol{x}^{\mathbf{fr}}$ should be a dimension to the minimization problem. In practice, when considering travelling waves, floes of reasonable size, and the succession of such quasi-static states, at most one single fracture is admissible at a given timestep, which greatly diminishes the numerical cost of the procedure. In what follows, we will thus use $N_{\rm fr} = 1$, $\boldsymbol{x}^{\mathbf{fr}} = \{x_1\}$, and we will have

$$E_{\rm el}^s = E_{\rm el}^< + E_{\rm el}^> \tag{13}$$

with $E_{\rm el}^<(x_1), E_{\rm el}^>(x_1)$ the elastic energies of the left ($x < x_1$) and right ($x > x_1$) fragments obtained from that single fracture, while the fracture energy reduces to $E_{\rm fr} = G$. Hence, we look for

$$\begin{cases} x_{\rm fr} = \underset{x_1 \in (0,L)}{\arg\min} \left(E_{\rm el}^< + E_{\rm el}^>\right), & \text{(14a)} \\ F(x_{\rm fr}) < 0. & \text{(14b)} \end{cases}$$

A fracture search is represented in Fig. 2. The asymmetry of the total energy profile comes from differences in wave phase at the edges of the floe, and wave attenuation by the ice cover, discussed in Sect. 2.3.

2.2.2 Strain criterion

To allow future comparisons, we additionally implement a conventional strain criterion for fracture. Under that formulation, the floe is allowed to fracture if the bending strain ε locally exceeds a prescribed critical strain $\varepsilon_{\rm cr}$, that is if

$$\exists x \mid \left|\varepsilon(x)\right| > \varepsilon_{\rm cr} \tag{15}$$

with

$$\varepsilon(x) = -\frac{h}{2}\frac{\mathrm{d}^2 w}{\mathrm{d}x^2} \tag{16}$$

the maximum (when taking the absolute value) bending strain, here defined as evaluated at the top of the floe.

Typically, if Eq. (15) holds anywhere, it holds on continuous intervals along the floe. We illustrate this in Fig. 3. A second criterion must then be chosen to constrain the fracture. Herein, we arbitrarily choose to consider the global strain extremum (single fracture). We thus have

$$\begin{cases} x_{\rm fr} = \underset{x \in (0,L)}{\arg\max} |\varepsilon(x)|, & \text{(17a)} \\ |\varepsilon(x_{\rm fr})| > \varepsilon_{\rm cr}. & \text{(17b)} \end{cases}$$

This criterion can be straightforwardly extended to the case of multiple fracture by considering all the local extrema exceeding the critical value.

https://doi.org/10.5194/egusphere-2025-1831
Preprint. Discussion started: 3 June 2025

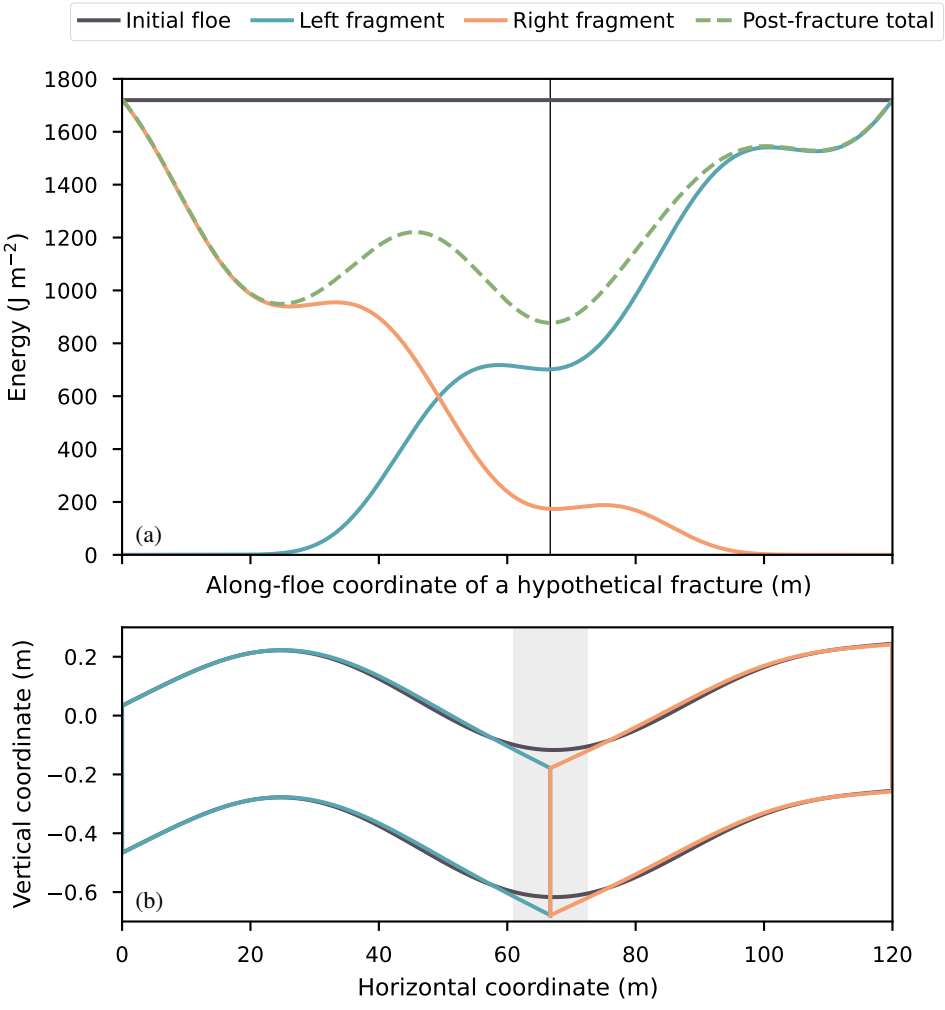

Figure 2. Illustration of a fracture search, from a situation corresponding to Fig. 1. In (a), contributions to the system's elastic energy change according to the coordinate of the fracture, and the total energy (that includes the fracture energy) is compared to the energy of the initial, unfractured floe in order to determine whether fracture should occur. The vertical line locates the global minimum, x_{fr}, of total energy which is, according to our model, where the floe should break. In (b), representation of the deformed floe, before and after fracture at x_{fr}. The shaded rectangle represents the energy relaxation length, as defined in Eq. (27), centred on x_{fr}.

https://doi.org/10.5194/egusphere-2025-1831
Preprint. Discussion started: 3 June 2025

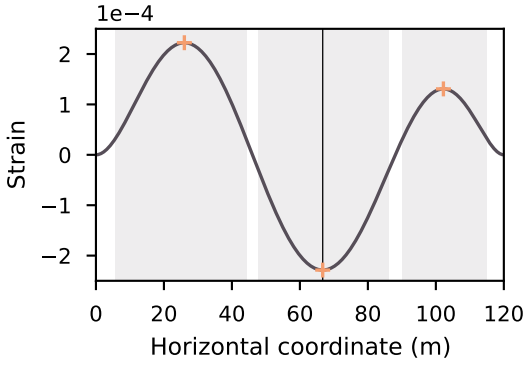

Figure 3. Strain-based fracture parameterisation, for a situation corresponding to Fig. 1. The line represents the maximum bending strain along the floe. The shaded vertical strips indicate where the strain exceeds, in absolute value, a typical critical strain of $\varepsilon_{\mathrm{cr}} = 3 \times 10^{-5}$. The crosses indicate local extrema, and the vertical line the global extrema.

2.3 Forcing waves

The main focus of this study being ice deformation and fracture, the wave component of the model is kept relatively simple. To align with the linearity hypothesis made on elastic plates, we only consider linear plane waves. This is also in line with previous studies (for instance, Kohout and Meylan, 2008; Dumont et al., 2011; Horvat and Tziperman, 2015).

2.3.1 Dispersion relations

For a prescribe angular frequency ω, we derive wavenumbers k from the dispersion relations

$$\frac{\omega^2}{g} = k \tanh(kH) \tag{18}$$

in the open-water parts of the domain, and

$$\frac{\omega^2}{g} = \left(\frac{D}{\rho_w g} k^4 + 1 - \frac{\omega^2}{g} d \right) k \tanh\big(k(H-d)\big) \tag{19}$$

in the ice-covered parts. We use the single symbol k for brevity, and the appropriate dispersion relation should be understood from context. In the right-hand side of Eq. 19, the term $\frac{D}{\rho_w g} k^4$ corresponds to the elastic response of the ice cover, while the term $\frac{\omega^2}{g} d$ corresponds to its mass-loading response. Whether the former has a significant contribution to the dispersion relation when the ice is heavily fragmented is debated (Sutherland and Dumont, 2018; Dumas-Lefebvre and Dumont, 2023). As it can easily be turned off, we include it here for completeness.

We note that this relation dispersion can be derived by considering the bending of a plate conforming to a fluid surface excited by harmonic waves. This can therefore be seen as a soft coupling of the fluid to the plate. The dispersion relation of plate excited by harmonic waves, without a fluid foundation, would otherwise be $\omega^2 = \frac{D}{\rho_i h} k^4$.

https://doi.org/10.5194/egusphere-2025-1831
Preprint. Discussion started: 3 June 2025

2.3.2 Wave state

For any given floe in the domain, a linear monochromatic wave can be parameterised with two complex variables, amplitude $\hat{a}$ and wavenumber $\hat{k}$. The modulus $a = |\hat{a}|$ denotes the amplitude of the wave at the left edge of the floe, while the argument $\phi = \mathrm{Ang}\,\hat{a}$ denotes the phase of that wave mode at the left edge of the floe. The real part of the wave number, $k = \mathrm{Re}\,k$, describes wave propagation while its imaginary part $\alpha = \mathrm{Im}\,\hat{k}$ describes the spatial rate of attenuation in the direction of propagation. Following Sutherland et al. (2019), we parameterise this attenuation to be linear in ice thickness and quadratic in wave frequency, so that

$$\alpha = \frac{1}{4} h k^2. \tag{20}$$

Other parametric attenuations can easily be added to the current framework, or attenuation turned off altogether.

A linear polychromatic plane wave can be defined by superposition. The wave state is then

$$\eta(x) = \sum_j \mathrm{Im}[\hat{a}_j \exp(\hat{k}_j x)] \tag{21}$$

where the subscript j denotes spectral modes. The modal amplitudes can be derived from any spectral density $S(\omega)$, using the relationship (Horvat and Tziperman, 2015)

$$\frac{1}{2} a_j^2 = S(\omega_j) \Delta\omega_j \tag{22}$$

where $\Delta\omega_j$ is the width of the angular frequency bin corresponding to the amplitude a_j.

2.3.3 Wave propagation over a finite distance

To allow for the advection of a developing sea into the ice-covered domain, we apply a semi-normal kernel to the sea state. We implement this modification to avoid the non-realistic situation of a fully developed sea appearing under a potentially kilometre-wide MIZ. Therefore, Eq. (21) is modified into

$$\eta(x) = \sum_j \mathrm{Im}\big[\hat{a}_j \exp(\hat{k}_j x)\big] K_j(x) \tag{23}$$

with

$$K_j(x) = \begin{cases} \exp\left(-\frac{(x-\mu_j)^2}{2{\sigma_j}^2}\right) & x \geq \mu_j, \\ 1 & x \leq \mu_j. \end{cases} \tag{24}$$

To each wave mode, we associate a coordinate μ_j. The wave is considered fully developed in the half-plane left of that coordinate. The parameters σ_j control the width of the transition between a fully developed wave, and a near-rest state (as the wave envelop of a given mode is reduced to about $0.01\,\%$ of its maximum at $x = \mu_j + 3\sigma_j$).

https://doi.org/10.5194/egusphere-2025-1831
Preprint. Discussion started: 3 June 2025

2.4 Numerical scheme

We have so far presented our framework for modelling fracture in a quasi-static state. Here, we give more details on how we iterate from a quasi-static state to the next, and summarise the steps leading to evaluating ice floe fractures.

2.4.1 Wave propagation–attenuation

Let τ be a model timestep. Each wave mode in Eq. (23) propagates at a phase speed

$$c_j = \frac{\omega_j}{k_j}. \tag{25}$$

Between time t_n and time t_{n+1}, the phase ϕ_j of mode j increases by $-\omega_j \tau$. The limit μ_j of the fully developed wave advances of a distance $c_j \tau$. Therefore, we iterate in time by updating the values of our $\hat{a}_j$ and μ_j by these quantities. A new quasi-static wave profile $\eta(x)$ can then be computed across the domain.

2.4.2 Sea ice deformation and fracture

Once the sea surface has been computed, the resulting sea ice deflection $w(x)$ is computed for all individual floes, which are scanned for possible fractures.

For a given floe, if $\mu_j > L \; \forall j$ (that is, the wave acting on the floe is fully grown), the deflection can be determined analytically, as developed in Appendix A. Otherwise, we obtain a solution with a numerical solver (Virtanen et al., 2020). In turn, the deflection is used to compute the curvature. Depending on the chosen fracture mechanism (energy-based or strain-based), the floes are considered for breakup, as described in Sect. 2.2.1 and 2.2.2.

If using the energy criterion, we evaluate the post-fracture total energy along the discretised floe. We use a peak detection algorithm (Virtanen et al., 2020) to separate intervals of convex free energy (as can be identified in Fig. 2a), onto which Eq. (13) is minimised. If the global minimum among these local minima satisfies Eq. (14b), fracture occurs.

If using the strain criterion, we evaluate the bending strain along the discretised floe. Again, a peak detection algorithm is run on $-\varepsilon^2(x)$ to detect convex intervals, and we conduct local minimization on these, which is equivalent to maximising $|\varepsilon(x)|$. If the global minimum satisfies Eq. (17b), fracture occurs.

2.4.3 Timestep selection

Care must be taken when selecting a model timestep, τ. The theoretical upper limit for crack propagation in an elastic, isotropic, and homogeneous material is set by the speed of Rayleigh waves, $c_\mathrm{R} = \sqrt{\frac{Y}{2\rho_i(1+\nu)}}$. Using values of the Young's modulus and Poisson's ratio estimated in situ for sea ice (for example, Moreau et al., 2020b), it is on the order of $c_\mathrm{R} \approx 1500\,\mathrm{m\,s^{-1}}$. As we consider cracks to instantaneously fracture floes through their thickness, we must have $\tau > \frac{h}{c_\mathrm{R}}$. For $1\,\mathrm{m}$ thick ice, it corresponds to $\tau > 6.67 \times 10^{-4}\,\mathrm{s}$.

However, we also want to keep the timestep small enough that we can detect fractures as soon as it is possible for them to occur, as delaying the onset of a fracture may affect the length of the resulting floes. Therefore, we aim to keep the ratio of

https://doi.org/10.5194/egusphere-2025-1831
Preprint. Discussion started: 3 June 2025

the progression of the wave front to the wave amplitude small. In the monochromatic case, with phase speed c, it translates to having $\frac{\tau c}{a} < r \Leftrightarrow \tau < r\frac{ak}{\omega}$, with $r < 1$. Setting $r = \frac{1}{5}$ ensures sufficient convergence. Analogous relationships can be derived for polychromatic cases.

3 Numerical experiment

To evaluate the capabilities of our model, and highlight the difference between energy and strain criteria, we choose to replicate breakup experiments conducted at the laboratory scale on an analogue material (Auvity et al., 2025). These focused on quantifying the onset of breakup, by progressively increasing the amplitude of a forcing wave, at different frequencies. The experiment setup was as follows: a water tank of length $80\,\mathrm{cm}$ and depth $11\,\mathrm{cm}$ was covered with a brittle layer of varnish, with thickness on the order of $100\,\mu\mathrm{m}$. The layer was detached from the walls of the tank prior to the experiment. Stationary surface waves were generated with a wave maker. A one-dimensional profilometry system and image-processing method were used to extract the wave properties (frequency, amplitude, wavenumber) and determine when fracture occurred.

As we aim to replicate this experiment, in what follows, we will be using a standing wave forcing and turn attenuation off. We use our model to determine, for prescribed wavenumbers and material properties inherited from these laboratory experiments (listed in Table 1), the critical amplitude a_{cr} at which the material starts to fracture. We do so using our energy formulation. Our model being linear, the amplitude directly controls the deflection of the plate, and thus, its curvature and elastic energy. It is therefore an intuitive quantity to control the outputs of the model, as well as a quantity that was measured experimentally.

The critical amplitude can then be related to a critical curvature κ_{cr} by evaluating Eq. (8) at the coordinate of the fracture. In turn, κ_{cr} can be used to derive a critical strain, using Eq. (16). We do not run separate experiments based on a strain criterion, as per the results of these authors, a constant critical strain does not exist for this material and therefore cannot be prescribed in our model. Even so, the results of energy-based simulations allow us to draw conclusions on the relevance of this type of criterion.

3.1 Length scales

To replicate the experimental protocol of Auvity et al. (2025), we consider only monochromatic stationary forcings, so that $\eta(x) = a\sin(k_n x)$ with $k_n = \frac{n\pi}{L}$. The symbol L represents both the length of the plate, and of the domain. The positive integer n is the harmonic number. The wave tank we simulate is short enough for attenuation to be considered insignificant.

We define two additional lengths: the flexural length

$$L_D = \left(\frac{D}{\rho_w g}\right)^{1/4}, \tag{26}$$

and the relaxation length

$$L_\kappa = \frac{\int_0^{x_{\mathrm{fr}}} (x_{\mathrm{fr}} - x)\left[\kappa(x) - \kappa^{<}(x)\right]^2 \mathrm{d}x}{\int_0^{x_{\mathrm{fr}}} \left[\kappa(x) - \kappa^{<}(x)\right]^2 \mathrm{d}x} + \frac{\int_{x_{\mathrm{fr}}}^{L} (x - x_{\mathrm{fr}})\left[\kappa(x) - \kappa^{>}(x)\right]^2 \mathrm{d}x}{\int_{x_{\mathrm{fr}}}^{L} \left[\kappa(x) - \kappa^{>}(x)\right]^2 \mathrm{d}x}. \tag{27}$$

https://doi.org/10.5194/egusphere-2025-1831
Preprint. Discussion started: 3 June 2025

The former is a natural length scale of our system, appearing in the bending equation (Eq. (6a)), and relates the flexural rigidity of the plate (that resists bending) to the reaction of the fluid it rests upon (that sustains bending). The latter gives a measure of the distance over which the curvature of post-fracture fragments is different from the curvature of the original floe that gave rise to these fragments. We show an example in Fig. 2b.

We introduced the symbols $\kappa^{<}(x)$ and $\kappa^{>}(x)$ to denote the curvature of the left and right post-breakup fragments, with $x \in [0, L]$. By definition, $\kappa^{<}$ (respectively $\kappa^{>}$) exists only for $x \in [0, x_{\mathrm{fr}}]$ (respectively $x \in [x_{\mathrm{fr}}, L]$). We choose this integral definition of L_κ because the differences in pre- and post-breakup curvatures is well-represented (when moving away from the fracture location) by a damped sine with oscillation period and attenuation rate $\sqrt{2}L_D$, that is,

$$\kappa(x) - \kappa^{>}(x) \sim \sin\Big(\frac{x}{\sqrt{2}L_D}\Big) \exp\Big(-\frac{x}{\sqrt{2}L_D}\Big), \tag{28}$$

which ensues from the shape of the solution presented in Appendix A1. Therefore, except at the floe boundaries where curvature is $0\,\mathrm{m}^{-1}$ (as imposed by the boundary condition, Eq. (6b)), the whole length of the initial floe may participate in releasing energy. For long enough waves, the relaxation length tends to $\sqrt{2}L_D$, that is $\lim_{k\to 0} L_\kappa = \sqrt{2}L_D$. This can be shown analytically by assuming Eq. 28.

We thus have three typical horizontal length scales:

- The wavelength $\lambda = \frac{2\pi}{k}$, imposed by the wave forcing, and linearly tied to the domain length L through the harmonic number n, so that $L = \frac{n\lambda}{2}$.
- The flexural length L_D, that depends on the properties of the material, the density of the fluid, and gravity. Only the former are varied in this study, with stiffer, thicker materials having a longer L_D.
- The relaxation length L_κ, that quantifies the distance over which fracture modifies the system.

3.2 Linearity limitation

The analogue material used in the laboratory experiments of Auvity et al. (2025) requires non-linear waves for fracture to occur. As neither non-linear plate nor non-linear waves are represented by our numerical model, we have to relax this condition, typically quantified by the wave slope ak, to observe fracture at all. Thus, we set the upper bound of our dichotomic searches so that $ak \leq 0.5$, which places us out of the linear framework our model relies on. As here, we are qualitatively showcasing the behaviour of our model rather than quantitatively exploiting the results, we deem this limitation to be inconsequential. For thickness and Young's modulus typical of sea ice, fracture in our model does happen in a linear regime, as illustrated in Fig. 2, where $ak = 0.015$.

Note that we define wave slope with respect to the wave propagating underneath the elastic plate and not with respect to the free surface waves. For a given time period, hydroelastic waves with dispersion relation Eq. (19) are typically longer than free surface gravity waves with dispersion relation Eq. (18), making the former slightly less steep.

https://doi.org/10.5194/egusphere-2025-1831
Preprint. Discussion started: 3 June 2025

Table 1. List of model parameters and their values. Parameters followed by an asterisk are inferred from other fixed parameters.

Parameter	Value
density (fluid)	$1000\,\mathrm{kg\,m^{-3}}$
density (plate)	$680\,\mathrm{kg\,m^{-3}}$
energy release rate	$174\,\mathrm{mJ\,m^{-2}}$
flexural length*	$7.50\,\mathrm{mm}$
flexural rigidity	$3.1 \times 10^{-5}\,\mathrm{Pa\,m^3}$
harmonic number	3
Poisson's ratio	0.4
thickness	$158\,\mu\mathrm{m}$
wavenumbers	21.0 to $203\,\mathrm{rad\,m^{-1}}$
Young's modulus*	$79.2\,\mathrm{MPa}$

4 Results

The results presented in this section focus on detecting a fracture threshold, using our energy formalism, and material parameters issued from a laboratory experiment. As we are interested in detecting the fracture threshold, and our model does not have a fatigue term, we work with strictly unrelated quasi-static states, and we find the critical amplitude a_{cr} systematically by dichotomic search. In Sect. 4.1, we detail the influence of varying the wavenumber exclusively. Then, in Sect. 4.2, we replicate the same protocol, while also varying the mechanical parameters of the plate.

4.1 Reference case

We start by illustrating the response of our model, for a range of prescribed wavenumbers, with four quantities: the normalised position of the fracture $\frac{x_{\mathrm{fr}}}{L}$, the critical amplitude and curvature, and the relaxation length. These are presented in Fig. 4. To exemplify the deviation between our computed deflection field and the forcing fluid surface, we choose here the case of the third harmonic, so that $L = \frac{3\pi}{k}$. We thus obtain curvature profiles that are symmetric[1] with respect to $x = \frac{L}{2}$, with three antinodes, which can be seen in Fig. 5. From left to right, the first and third antinodes (close to the left and right edges of the plate, respectively) are more influenced by the boundary conditions than the second one (located at the middle of the plate). We give the model parameters in Table 1.

In what follows, we multiply k by the flexural length, so that to obtain the (dimensionless) wavenumber kL_D. This allows exploring the model behaviour between two limits: small kL_D values thus correspond to longer waves and lower flexural rigidity (the plate conforms to the fluid), while high values correspond to shorter waves and higher flexural rigidity (the plate is non-deformable). We divide Fig. 4b–d in four regions, based on different behaviours of the fracture location as predicted by

[1] As would be the case for any odd harmonic number. In the case of even harmonic number, the curvature profile as a twofold rotational symmetry about $(x, \kappa) = \left(\frac{L}{2}, 0\right)$. In other words, $\kappa\left(x - \frac{L}{2}\right)$ is even-symmetric for odd harmonic wavenumbers, and odd-symmetric for even harmonic numbers.

https://doi.org/10.5194/egusphere-2025-1831
Preprint. Discussion started: 3 June 2025

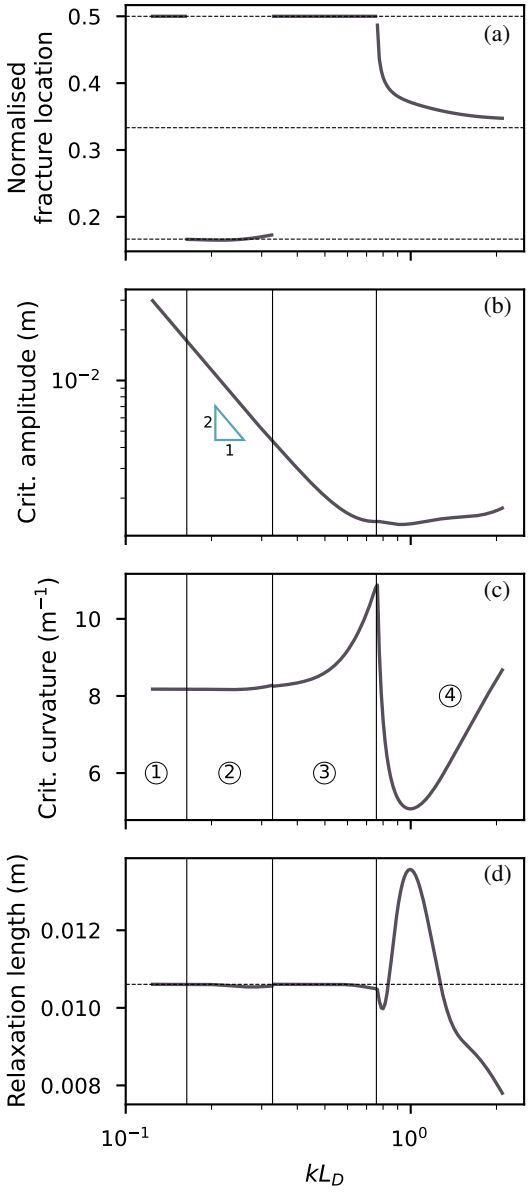

Figure 4. Relationships between the nondimensionalised wavenumber and normalised (with respect to plate length) fracture location (a), critical amplitude (b), critical curvature (c), and relaxation length (d). Model parameters are provided in Table 1. In (a), three horizontal dashed lines represent the asymptotes $\frac{x_{\mathrm{fr}}}{L} = \frac{1}{6}$, $\frac{1}{3}$ and $\frac{1}{2}$. In (b) to (d), vertical lines show delimitations between regions corresponding to different behaviours of fracture location, observed on (a). The regions are numbered in (c). In the second region of (b), the triangle of height twice its horizontal base (in loglog space and data units) gives an indication of the slope. In (d), an horizontal dashed line represents the asymptote $\sqrt{2}L_D$.

https://doi.org/10.5194/egusphere-2025-1831
Preprint. Discussion started: 3 June 2025

the energy criterion, identified in Fig. 4a. These regions are separated by $kL_D = 0.1638,\ 0.3275$ and 0.7578. They correspond, for increasing kL_D, to fracture happening in the middle of the floe (the second curvature antinode); fracture happening close to the first or third curvature antinode; fracture again happening in the middle of the floe; and fracture uncorrelated from any curvature extremum. Because of the particular wave forcing imposed in our model configuration, the free energy profile is symmetrical with respect to the middle of the plate. Therefore, it is not numerically possible to discriminate between an energy minimum happening at x_{fr} or $L - x_{\mathrm{fr}}$, and in Fig. 4a, we only show the branch corresponding to $x_{\mathrm{fr}} \leq \frac{L}{2}$.

We note that, in regions 1 to 3, fracture predicted by the energy criterion does not systematically happen at the global curvature extrema. In this third harmonic case, the global extremum is in the middle of the floe, except in the band $kL_D \in [0.178, 0.357]$. The overlap with the region 2, defined by $kL_D \in [0.1638, 0.3275]$, is thus not one-to-one. Additionally, in region 2, fracture does not happen at the antinode, but in its vicinity. For $kL_D < 0.242$, fracture is on the left of the first antinode, and for $kL_D > 0.243$, to its right (the situation is reversed for the third antinode). In region 4, fracture happens far from either antinode. It seems that for increasing kL_D, $\frac{x_{\mathrm{fr}}}{L} \to \frac{1}{3}$, which corresponds to a node of the forcing.

In Fig. 5, we show examples of the behaviour of the free energy and of the along-plate curvature for these different regions. We compare the latter to the "conforming" curvature, $\kappa_{\mathrm{conf}}(x) = \frac{\mathrm{d}^2}{\mathrm{d}x^2} w_{\mathrm{conf}}$, with $w_{\mathrm{conf}}(x) = \frac{a}{1+(kL_D)^4} \sin(kx)$ the associated displacement stemming from the fluid surface. The term at the denominator ensures that it satisfies Eq. (6a), and for long waves, $\lim_{k \to 0} w_{\mathrm{conf}} = \eta$. In Fig. 6, we show for the same examples the floe deflection, compared to the forcing amplitude, and we indicate the relaxation length. To aid comparison, we normalise the along-floe coordinate by the floe length.

In the first two regions, both corresponding to small wavenumbers, the difference between curvature and conforming curvature (Fig. 5a, Fig. 5b) is noticeable only in the immediate vicinity of the edges of the domain. Minima of free energy correspond roughly with extrema of curvature, and the floe deflection (Fig. 6a, Fig. 6b) follows the fluid surface. In the first region, and to a lesser degree in the second region, the critical curvature (Fig. 4c) varies little, although a slight positive trend exists. Our strain-based and energy-based criteria in these two regions would therefore predict virtually similar fractures. The critical amplitude (Fig. 4b) varies with the inverse of the squared wavenumber, that is, with the square of the wavelength. The relaxation length (Fig. 4d) is almost constant and tends to $\sqrt{2}L_D$ from below for decreasing wavenumbers. As the floe length is, in the case of stationary wave forcing, inversely proportional to the wavenumber, the relaxation length *normalised* by the floe length increases with the wavenumber, and is not constant across the different panels of Fig. 6.

In the third region, curvature and conforming curvature (Fig. 5c) are now dissimilar between the left (respectively right) edge and the left (respectively right) antinode. The free energy still shows three troughs, but the trough at $x = \frac{L}{2}$ is now clearly more pronounced than the other two. There are still three distinct deflection extrema (Fig. 6c), synchronised with the forcing wave, and the amplitude of deflection of the floe is slightly smaller than the forcing amplitude. From $kL_D \approx 0.3057$, we locally (around the two positive deflection antinodes) have $\eta - w > h - d$. As $h - d$ corresponds to the freeboard of the floe at rest, this suggests parts of the deformed floe are immersed. This takes place close to the transition from the second region, which happens at $kL_D = 0.3275$. The non-zero deflection near the edges shows that deflection is now significantly different from the sine forcing. In terms of the occurrence of fracture, this region corresponds to a sharp increase in critical curvature, incompatible with a strain-based (that is, constant critical curvature) criteria. The relaxation length, however, is still practically

https://doi.org/10.5194/egusphere-2025-1831
Preprint. Discussion started: 3 June 2025

constant with kL_D, and a good indicator of the zone over which pre- and post-fracture modelled deflection differ. An inflexion of the critical amplitude decrease rate is also visible. In regions 1 to 3, fracture locations near antinodes and the shape of post-fracture deflections are consistent with mode I fracturing.

As kL_D increases, the length of the plate diminishes relatively to its flexural length. The impact of the boundary conditions on the deflection profile is therefore amplified. This effect is sizeable in the fourth region (Fig. 6d): curvature and conforming curvature (Fig. 5d) no longer match anywhere along the plate. This is despite staying in a regime where $L_D \gg L$, as $kL_D = n\pi\frac{L_D}{L} \approx 10\frac{L_D}{L}$. The central free energy trough has separated into two distinct troughs corresponding to global minima, no longer in phase with curvature extrema. This separation corresponds to the transition from the third region. The fourth region also shows a drop in critical curvature (Fig. 4c), which has been monotonically increasing with kL_D thus far. However, the maximum curvature $\kappa(L/2)$ keeps increasing irregularly with kL_D, as can be seen by comparing Fig. 6c and Fig. 6d. The critical amplitude, which seems to plateau on the right of the third region (Fig. 4b), is singular at the transition, then diminishes again before increasing irregularly. Additionally, the edges of the fragments no longer mirror each other. There is a significant post-fracture discontinuity in deflection, which is a characteristic of region 4, and not consistent with bending (mode I) fracture, but reminiscent of a sliding (mode II) or tearing (mode III) fracture. A minimum of critical curvature is reached for $kL_D = 1$, which also corresponds to a maximum of relaxation length. For $n \geq 2$, there is a single positive kL_D, quickly converging to 1, for which the slope at the edges of the floe vanishes, that is, $\left(\frac{\mathrm{d}w}{\mathrm{d}x}\right)_{x=0,L} = 0$. It corresponds to the two outside-most deflection antinodes vanishing, leaving only the internal ones. It can be seen from the deflection profile in Fig. 6d, that compared to Fig. 6a–c, the slope at the edges has changed sign, and that a single antinode (at the centre of the floe) remains.

4.2 Influence of mechanical parameters

We further investigate the response of our model to varying mechanical parameters, by reproducing the analysis presented in Sect. 4.1 for an ensemble of (h, Y) pairs with 128 members. Doing so, we aim to reproduce the internal variability that stems from laboratory conditions in the experiments of Auvity et al. (2025). We generate this ensemble through Latin hypercube sampling, and enforce that the two variables are independent with normal marginal densities of prescribed means $100\,\mu\mathrm{m}$ and $70\,\mathrm{MPa}$, and prescribed standard deviations $20\,\mu\mathrm{m}$ and $14\,\mathrm{MPa}$, respectively; we show the joint density of our sample in Fig. 7. The resulting distribution of flexural rigidities is positively skewed, with mean $7.88 \times 10^{-6}\,\mathrm{Pa\,m^3}$ and median $6.93 \times 10^{-6}\,\mathrm{Pa\,m^3}$.

We further impose the relation

$$\frac{2Gh^2}{D} = C \tag{29}$$

between the energy release rate, the Young's modulus, and the thickness, as derived by Auvity et al. (2025), setting the dimensionless material constant parameter $C = 2.8 \times 10^{-4}$. This expression serves as a proxy establishing a value for G, which is poorly constrained experimentally. The other parameters are kept fixed at the values presented in Table 1. We also keep the same constraint on the wave slope, requiring $a_{\mathrm{cr}}k \leq 0.5$: depending on the precise values assumed by the thickness and Young's modulus, the interval of wavenumbers that leads to fracture may vary.

https://doi.org/10.5194/egusphere-2025-1831
Preprint. Discussion started: 3 June 2025

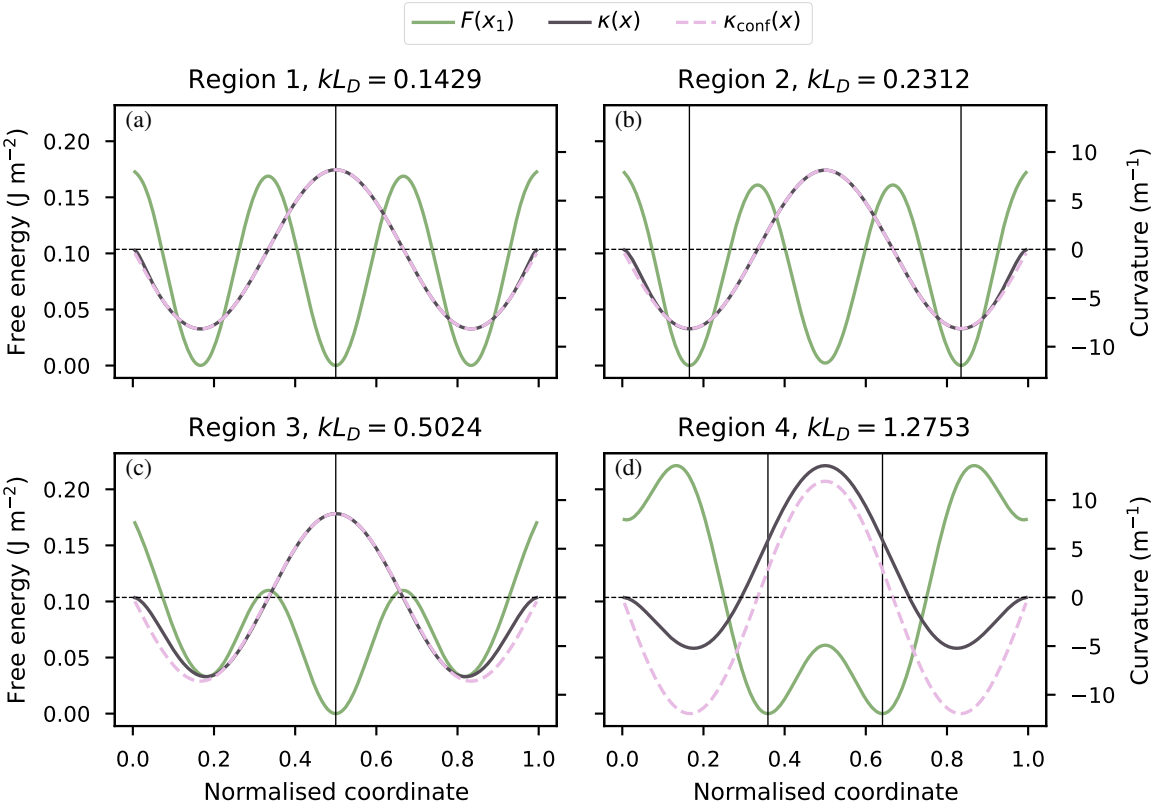

Figure 5. Examples of free energy (left vertical axes, green lines) and curvature (right vertical axes, grey lines) profiles for the four regions identified in the text. A sine curvature is shown in dashed lines as a comparison to the curvature derived from Eq. (8). The fracture locations, determined from the energy criterion, are shown with vertical lines: the energy profiles being symmetrical with respect to the middle of the plates, $F(x_{\text{fr}}) = F(L - x_{\text{fr}})$. The dashed horizontal lines show the zero-curvature reference.

4.2.1 Comparison to experimental data

We show numerical results in Fig. 8 (colour-coded lines), which we compare to experimental data from Auvity et al. (2025) (circle and square markers). We obtain results similar to those presented in Sect. 4.1. The critical amplitude profiles do not depend on the mechanical properties of the simulated material, up to a multiplicative constant, that increases with flexural rigidity (or, equivalently, flexural length).

This fact extends to the other variables shown in Fig. 4. Within the ranges of mechanical parameters explored, which are in agreement with the values and internal variability estimated by Auvity et al. (2025), the order of magnitude of the critical amplitude and its decreasing tendency with increasing kL_D agree between the simulations and the laboratory experiments. However, and as expected, this agreement is only qualitative. Indeed, we recall that in the experimental setting, fracture was only obtained with non-linear waves. It is likely the reason why the critical amplitudes measured by Auvity et al. (2025)

https://doi.org/10.5194/egusphere-2025-1831
Preprint. Discussion started: 3 June 2025

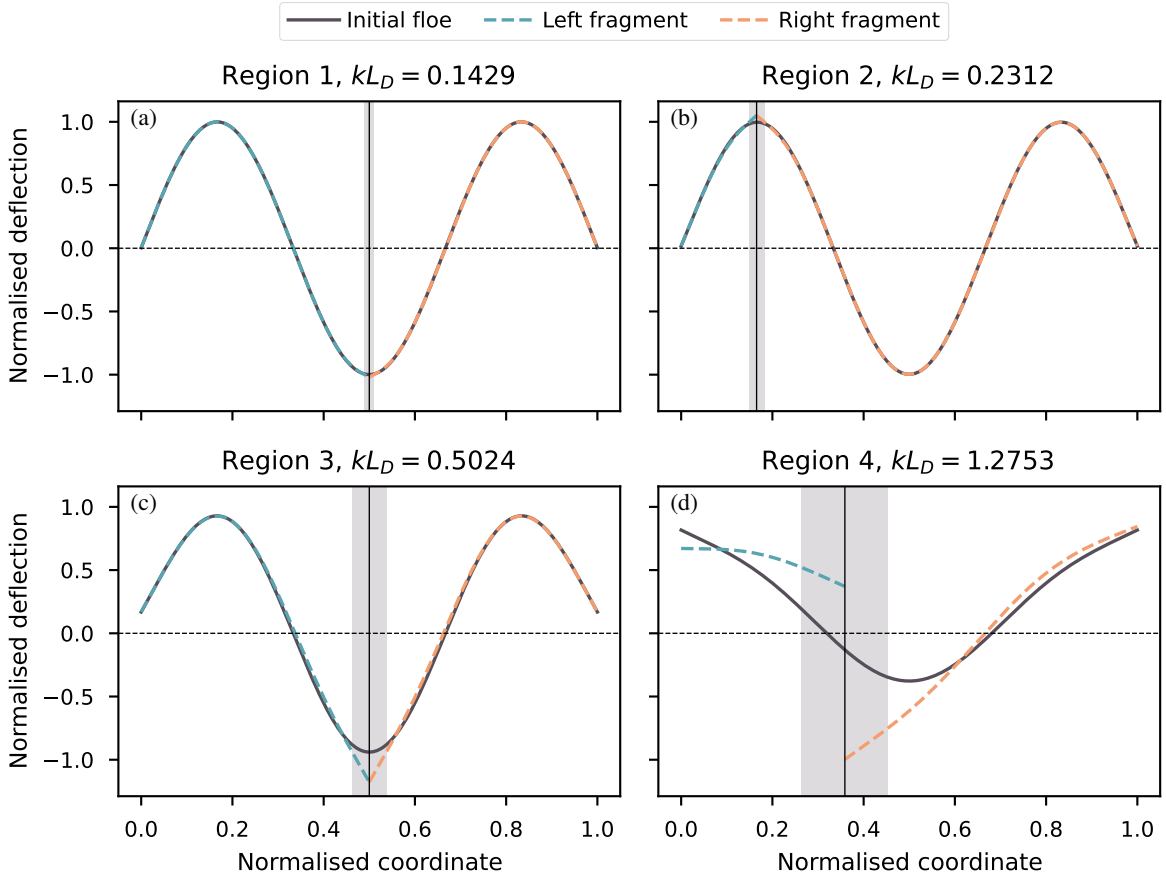

Figure 6. Examples of pre- and post-fracture floe deflection profiles for the four regions identified in the text, normalised by the critical amplitude. The relaxation lengths, centred on the fracture locations, are shown with shaded rectangles. We only consider the left fracture location, where applicable. The dashed horizontal lines show the zero-deflection reference.

varies as k^{-1}, not as k^{-2} as we find numerically. The differences between experimental and numerical critical amplitudes are therefore deepened at small wavenumbers.

We also note that the way we define the relaxation length L_κ in our linear waves simulations differs from the definition of Auvity et al., who used the full width at half-maximum (hereinafter, FWHM) of pre-fracture curvature in their nonlinear experiments. On Fig. 8, we thus also represent the experimental critical amplitudes as a function of $\frac{L_D}{\mathrm{FWHM}}$ (pink squares), which horizontally shifts the experimental points, in an attempt to correct the discrepancy between their nonlinear waves forcing and our linear model.

We do not adopt their definition, as it would be incompatible with our region 4 results, where fracture does not happen around curvature peaks or troughs, while experimental fractures always happened in the vicinity of a deflection antinode. If we were to apply it to regions 1 to 3, we would obtain something very similar to the FWHM of $\sin(kx)$, that is $\frac{2\pi}{3k}$, $\frac{\lambda}{3}$. Because of

https://doi.org/10.5194/egusphere-2025-1831
Preprint. Discussion started: 3 June 2025

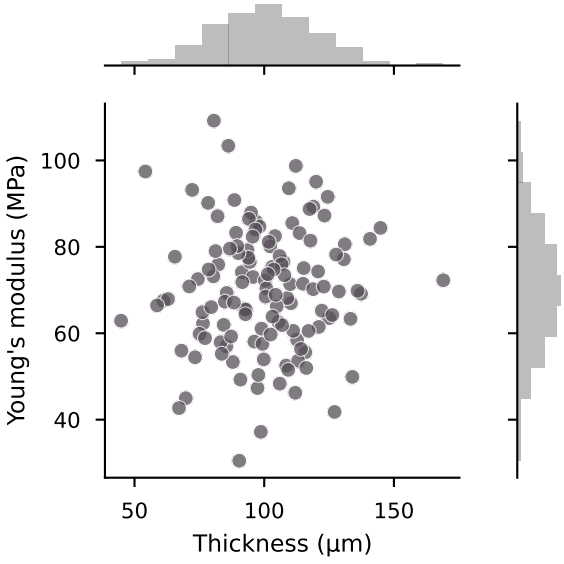

Figure 7. Joint density and marginal densities of our (h, Y) ensemble.

their nonlinear wave forcing, Auvity et al. measured FWHMs that varied like $\frac{\lambda}{12}$. Bending was thus concentrated in a smaller fraction of their forcing wavelengths, and $\frac{L_D}{\mathrm{FWHM}}$ can be seen as an alternative, rescaled dimensionless wavenumber. Using this definition, we can improve the overlap between experimental and numerical results, with experimental points falling in regions 1 to 3, where both model end experiments show the critical curvature depends on the forcing wavelength, precluding a constant strain threshold.

4.2.2 Impact of harmonic number and dimensionless quantities

So far, we focused on the harmonic number $n = 3$. However, for large enough kL_D, the response of the model depends on n, and therefore on the geometry of the domain. In particular, for even n, fracture in region 4 happens systematically in the middle of the floe. Due to the symmetry property of the forcing, this means our model predicts fracture with $\kappa_{\mathrm{cr}} = 0\,\mathrm{m}^{-1}$, inconsistent with bending fracture but reminiscent of shearing or tearing fracture. The fundamental configuration, with $n = 1$, is a particular case. The maxima of deflection, curvature, and free energy happen at $x = \frac{L}{2}$ independently of kL_D. We illustrate this difference in Fig. 9 by presenting the relationships between the nondimensionalised wavenumber and two dimensionless quantities, for different harmonic wavenumbers. We choose these two quantities because they exhibit the remarkable property of depending on the dimensionless wavenumber, but not on the individual variations of the mechanical parameters.

The first of these quantities, shown in Fig. 9a, is the relaxation length L_κ (as shown in Fig. 4d for the fixed parameters experiment), normalised by the augmented flexural length $\sqrt{2}L_D$. We retrieve, independently of the harmonic number, the limit $\lim_{k\to 0} L_\kappa = \sqrt{2}L_D$ already stated in Sect. 3.1. Behaviours depending on the harmonic number emerge from $kL_D \approx 0.4$.

https://doi.org/10.5194/egusphere-2025-1831
Preprint. Discussion started: 3 June 2025

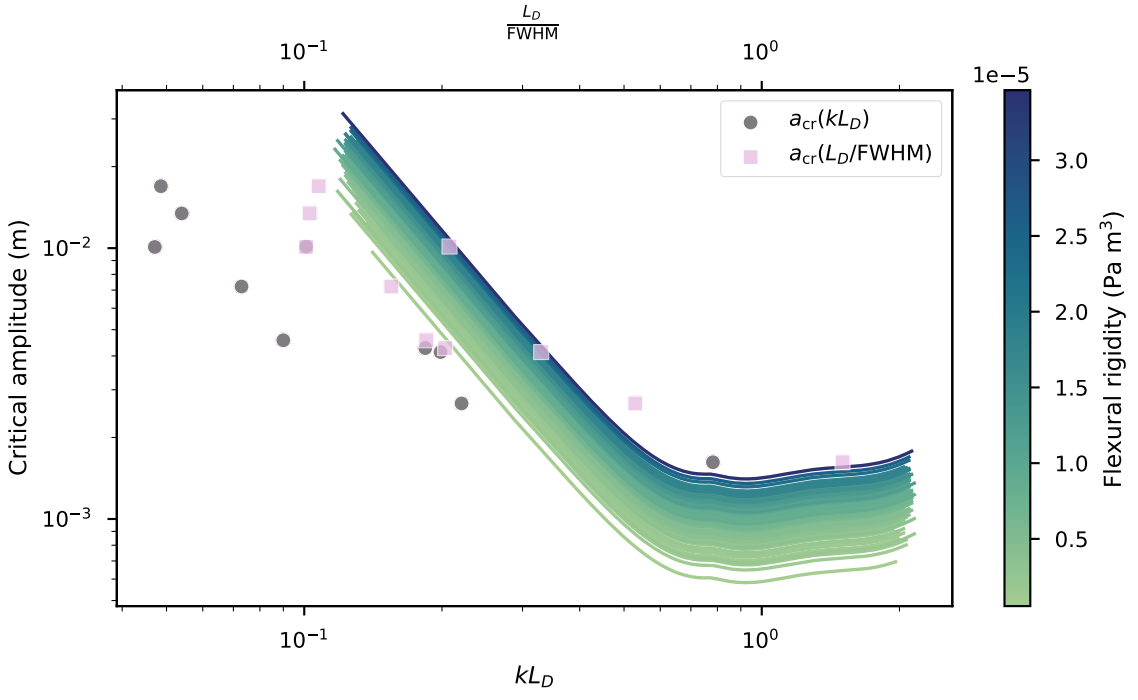

Figure 8. Relation between the dimensionless wavenumber and the critical amplitude, for varying thickness and Young's modulus. Lines are numerical results, with the colour scale indicating the flexural rigidity, that combines the two varying parameters. Grey dots are experimental results from Auvity et al. (2025). Pink squares are the same experimental results, with a different horizontal scaling, as described in the text.

If all curves show a downward trend in what corresponds to kL_D in regions 2 and 3, this trend is more pronounced for smaller numbers, in particular $n \in \{1, 2\}$. The second striking difference, is that between even and odd harmonic numbers. There is a discontinuity at the transition from region 3 to region 4 for even numbers, with an upward jump preceding a sustained downward trend. This transition is continuous for $n = 3$. There is no region 4 behaviour for $n = 1$, as in this configuration, fracture always happens at $\frac{x_{\mathrm{fr}}}{L} = \frac{1}{2}$.

The second dimensionless number, shown in Fig. 9b, can be built as the product of two distinct dimensionless quantities: critical curvature multiplied by thickness (that is, twice the critical strain), and critical curvature multiplied by relaxation length. Notably, both these quantities do depend on thickness and Young's modulus, without showing the ordering critical amplitude does in Fig. 8. However, their product, ${\kappa_{\mathrm{cr}}}^2 h L_\kappa$, only depends on kL_D. This quantity was also derived by Auvity et al. (2025), who interpreted it as a constant independent of the wave forcing. We do not replicate this result outside of regions 1 and 2, that is, the wavenumber band where neither critical curvature nor relaxation length vary. As in Fig. 9a, the different curves are indistinguishable within these two regions, i.e., at small kL_D and a discontinuity exists for even harmonic numbers between regions 3 and 4, as for these, the critical curvature drops to $0\,\mathrm{m}^{-1}$ in region 4.

https://doi.org/10.5194/egusphere-2025-1831
Preprint. Discussion started: 3 June 2025

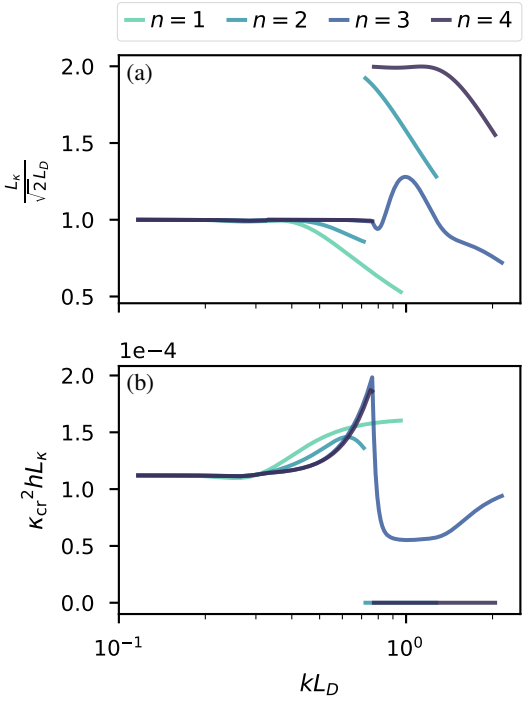

Figure 9. Relationship between the nondimensionalised wavenumber and two dimensionless quantities: the energy dissipation length scaled by the flexural length (a), and squared critical curvature scaled by thickness and flexural length (b). We show ensemble averages, for four harmonic numbers. For a given harmonic number, ensemble members are virtually identical, with coefficients of variation well below 1×10^{-3} where the means are non-zero.

Finally, it can be seen that the upper bound of the range of kL_D that sees fracture happens depends on n. It first increases with n but peaks for $n = 3$, and then decreases. This is despite keeping the same $a_{\text{cr}}k \leq 0.5$ criterion on the wave slope. The lower bound, however, does not change and keeps the value $kL_D = 0.1167$. The differences between the different harmonics in region 4 are explained by the loss of deflection extrema near the boundaries as kL_D increases, which have dissimilar effects on the deflection profile in this region for different n. For $n > 2$, there exists a single kL_D for which the slope of the deflection at the edges of the plate, $\left(\frac{\mathrm{d}w}{\mathrm{d}x}\right)_{x=\{0,L\}}$, cancels. It converges exponentially towards 1, so that noting it $(kL_D)_0$, we have $\log|1 - (kL_D)_0| \sim -n$. The cancellation of the slope conveys the transition from a deflection profile with n antinodes to one with $n-2$ antinodes. When kL_D keeps increasing, the higher n, the higher the variety of behaviours shown by w. However, for large enough kL_D, $w(x) \to \frac{2a}{n\pi}$ for odd n, and $w(x) \to \frac{2a}{n}\left(-\frac{2x}{L} + 1\right)$ for even n. These are rigid motions, independent of the forcing, corresponding respectively to heave (translation) or pitch (rotation).

https://doi.org/10.5194/egusphere-2025-1831
Preprint. Discussion started: 3 June 2025

5 Discussion and conclusion

We have developed a novel one-dimensional model that simulates the fracture of sea ice by waves. This model has the particularity of solving directly for the deflection of a floe caused by the competition between buoyancy and gravity; instead of solving for waves scattered by the presence of the floe at the ice–fluid interface, and assuming that the deflection follows that interface. We can thus use the model to continuously explore the response of a floe to bending, and fracture, between two limits: an elastic plate conforming exactly to a fluid foundation, and an undeformable plate. We have implemented two fracture criteria. One, compatible with continuum fracture mechanics, is based on looking for a global post-fracture energy minimum and comparing it to the pre-fracture energy state to determine whether fracture should occur, and is another novelty of this model. The other is compatible with the more common hydroelastic approach applied to sea ice, based on locally comparing strain to a prescribed threshold.

The present study is centred on presenting the theoretical and numerical aspects of the model itself. We apply the model to an analogue material used in the laboratory to study wave-induced ice fracture, in the specific setting of monochromatic stationary waves. Because no critical strain has been experimentally derived for this material, but a relationship between energy release rate and other parameters of our model exists, we focus on investigating the energy criteria. Even in this particularly simplified configuration, the response of the model in terms of critical amplitude or curvature is not straightforward.

Our results indicate that the critical curvature derived from an energy-based fracture depends on the forcing wave, contradicting the existence of a universal critical strain. This was also observed in the laboratory (Auvity et al., 2025). In the wavenumber kL_D band where our results overlap with the experimental data from Auvity et al. (2025), we obtain comparable critical amplitudes. However, we are not able to replicate their scaling for low wavenumbers kL_D. Additionally, we obtain that for large enough kL_D (region 4), the two criteria diverge on the predicted fracture location, in that energy-predicted fracture is uncorrelated from curvature, or strain, extrema. The fracturing behaviour in region 4 is inconsistent with bending fracture, and suggests out-of-plane shear or in-plane shear fracturing. The latter would describe fracture propagating perpendicularly to the direction of wave propagation (that is, as someone tearing up a sheet of paper), in contradiction with the invariance hypothesis made on the modelled plate and therefore cannot be represented in the current 1D model.

A possible explanation for the different relationship between critical amplitude and wavenumber observed experimentally ($a_{\mathrm{cr}} \sim k^{-1}$) and numerically ($a_{\mathrm{cr}} \sim k^{-2}$, for $kL_D \lesssim 0.6$) may be that experimentally, for fracture to happen, the material considered (varnish) required non-linear wave forcing, which our model does not represent. In the case of ice, the linearity assumption is, however, valid. For values corresponding to a similar experiment conducted on fresh water ice by the same team (personal communication with Auvity et al.), that is thicker and stiffer than their varnish, our results in terms of critical amplitude as a function of dimensionless wavenumber are, up to multiplicative constants, identical to those presented here, and the wave slopes required to obtain fracture are typically of the order of 0.02; well within the linear regime. Therefore, increasing the numerical complexity of the model to accommodate non-linear plate behaviour seems unnecessary at this stage. Another explanation is that, while our model considers homogeneous plates with constant Young's modulus, the material engineered by

https://doi.org/10.5194/egusphere-2025-1831
Preprint. Discussion started: 3 June 2025

Auvity et al. (2025) is obtained by layering. Because of introduced vertical inhomogeneities, this process is likely to introduce a dependency of the Young's modulus to the obtained thickness.

The key features of our model are that bending is driven exclusively by the along-plate variation of buoyancy, which cannot be resolved by hydroelastic models, and that fracture can be controlled by an energy criterion integrated over the entire floe. For high kL_D values, that is either large wavenumber or a stiff elastic plate, this leads to physically questionable behaviours, such as submergence, and post-breakup deflection discontinuity across the fracture (region 4) or even fracture at zero-curvature (for even harmonics). We note that the possibility of submergence is the direct consequence of the weak, one-way coupling between fluid and plate, as we only represent the response of the plate to the fluid, while ignoring the feedback response of the fluid. This one-way coupling is a trade-off allowing us to maintain the theoretical and numerical complexity low. As a rationality check, we verify that the bending energy, transmitted to the plate by the fluid, is orders of magnitude less than the gravitational potential energy of the fluid: there is thus no unaccounted energy leaks into the plate. As none of this energy is returned to the fluid, it is likely we overestimate the likeliness of fracture.

Here, we have described the simulated behaviour as a function of kL_D by distinguishing the results in 4 different regions, based on where the fracture happens. The kL_D thresholds being regions should however be regarded carefully, as they depends slightly on the harmonic number of the forcing, and might be a feature of stationary forcing. In typical field conditions, with waves propagating within the ice cover, the fracture front follows the wave front, in such a way that fragments are typically smaller than the dominant wavelength (Dumas-Lefebvre and Dumont, 2023). Therefore, the increased complexity in the model behaviour at high harmonic numbers may not be representative of natural conditions.

More experimental data is needed to confirm or infirm the behaviour of the model in the large kL_D band, and whether a forcing-dependent trend for critical curvature exists in the case of ice. Previous wave tank fracture experiments (Dolatshah et al., 2018) showed bending failure typically happening at $kL_D \approx 1$, though the uncertainties on thickness and Young's modulus are quite large. Other values of Young's modulus reported for such experiments, in the low MPa range (Herman, 2018; Passerotti et al., 2022), seem inconsistent with a uniform, solid sheet of ice, as represented in our model. In the case of realistic wave forcing, with material parameters representative of first-year sea ice, the peak of wave energy occurs in kL_D bands corresponding to what we identified as region 3 and 4. However, higher-frequency waves are also the ones most effectively attenuated by the ice cover, so that they contribute less to fracture. Planned future work will involve using our model to study whether the choice of fracturing criterion impacts the floe size distribution resulting from propagating wave-induced breakup.

Code and data availability. The current version of SWIIFT is available from the project website https://github.com/sasip-climate/swiift under the APACHE-2.0 licence. The exact version of the model used to produce the results used in this paper is archived on https://doi.org/10.5281/zenodo.15528673 (Mokus, 2025c). The input data and scripts to run the model and produce the plots for all the simulations presented in this paper are archived on https://doi.org/10.5281/zenodo.15528650 (Mokus, 2025b). A package dedicated to reproducing the figures, holding the necessary data but no model logic, is archived on https://doi.org/10.5281/zenodo.15230102 (Mokus, 2025a).

https://doi.org/10.5194/egusphere-2025-1831
Preprint. Discussion started: 3 June 2025

Appendix A: Equation for the moment-deformation

We consider the boundary problem

$$\begin{cases} \dfrac{\mathrm{d}^4 w}{\mathrm{d}x^4} = \sigma^4 \left[\eta(x) - w(x)\right] & x \in [0, L] \quad \text{(A1a)} \\ \dfrac{\mathrm{d}^2 w}{\mathrm{d}x^2} = 0 & x \in \{0, L\} \quad \text{(A1b)} \\ \dfrac{\mathrm{d}^3 w}{\mathrm{d}x^3} = 0 & x \in \{0, L\}. \quad \text{(A1c)} \end{cases}$$

where η denotes the surface undergoing wave forcing, w the floe deflection, and $\sigma = \frac{1}{L_D}$ is the reciprocate of the flexural length.

The surface η is typically the superposition of propagating, attenuated wave modes, so that

$$\eta(x) = \sum_j \eta_j(x) \quad \text{(A2)}$$

and

$$\eta_j(x) = a_j \exp(-\alpha_j x) \sin(k_j x + \phi_j), \quad \text{(A3)}$$

with a wave amplitude, α wave attenuation per unit distance, k wave number, and ϕ wave phase at the left floe edge. The index j is used with respect to a discretised wave spectrum.

Finally, we define the elastic energy per unit cross-sectional area

$$E = \frac{D}{2h} \int_0^L \left(\frac{\mathrm{d}^2 w}{\mathrm{d}x^2} \right)^2 \mathrm{d}x. \quad \text{(A4)}$$

In the rest of this document, we will note

$$\kappa(x) = \frac{\mathrm{d}^2 w}{\mathrm{d}x^2} \quad \text{(A5)}$$

the curvature of the floe.

The ODE (A1a) is linear, and so are the boundary conditions fourth order ODE, but it is linear, and so are the boundary conditions (A1b),(A1c). Here, we consider the simplified case where D and h are constant, making Eq. (A1a) a constant-coefficients, linear ODE.

A1 Solution to the BVP on the floe deflection

The ODE (A1a) is linear and non-homogeneous. Its general solution w is the superposition of an homogeneous solution w_h and a particular solution w_p.

https://doi.org/10.5194/egusphere-2025-1831
Preprint. Discussion started: 3 June 2025

A1.1 Homogeneous solution

The characteristic polynomial of the homogeneous ODE

$$\frac{\mathrm{d}^4 w}{\mathrm{d}x^4} + \sigma^4 w(x) = 0 \tag{A6}$$

associated with (A1a) is

$$P(s) = s^4 + \sigma^4. \tag{A7}$$

It has solutions

$$(1+\mathrm{i})\tilde{\sigma}, (1-\mathrm{i})\tilde{\sigma}, (-1+\mathrm{i})\tilde{\sigma}, (-1-\mathrm{i})\tilde{\sigma} \tag{A8}$$

with $\tilde{\sigma} = \frac{\sqrt{2}}{2}\sigma$. Independent solutions to (A1a) are thus

$$\check{\boldsymbol{f}} = \begin{bmatrix} \exp(\tilde{\sigma}x)(\cos(\tilde{\sigma}x) + \mathrm{i}\sin(\tilde{\sigma}x)) \\ \exp(\tilde{\sigma}x)(\cos(\tilde{\sigma}x) - \mathrm{i}\sin(\tilde{\sigma}x)) \\ \exp(-\tilde{\sigma}x)(\cos(\tilde{\sigma}x) + \mathrm{i}\sin(\tilde{\sigma}x)) \\ \exp(-\tilde{\sigma}x)(\cos(\tilde{\sigma}x) - \mathrm{i}\sin(\tilde{\sigma}x)) \end{bmatrix}. \tag{A9}$$

Applying the full-rank linear transformation

$$\frac{1}{2}\begin{bmatrix} 1 & 1 & 0 & 0 \\ -\mathrm{i} & \mathrm{i} & 0 & 0 \\ 0 & 0 & 1 & 1 \\ 0 & 0 & -\mathrm{i} & \mathrm{i} \end{bmatrix} \tag{A10}$$

to $\check{\boldsymbol{f}}$ yields the real-valued independent solutions

$$\boldsymbol{f} = \begin{bmatrix} \exp(\tilde{\sigma}x)\cos(\tilde{\sigma}x) \\ \exp(\tilde{\sigma}x)\sin(\tilde{\sigma}x) \\ \exp(-\tilde{\sigma}x)\cos(\tilde{\sigma}x) \\ \exp(-\tilde{\sigma}x)\sin(\tilde{\sigma}x) \end{bmatrix}. \tag{A11}$$

Finally, any linear combination $\boldsymbol{f}^T\boldsymbol{c}$, with the real-valued vector

$$\boldsymbol{c} = \begin{bmatrix} c_1, c_2, c_3, c_4 \end{bmatrix} \tag{A12}$$

is a solution to (A6).

https://doi.org/10.5194/egusphere-2025-1831
Preprint. Discussion started: 3 June 2025

A1.2 Particular solutions

The non-homogeneous term in (A1a) can be written

$$\sigma^4\eta(x) = \sigma^4 \sum_j \eta_j(x) \tag{A13}$$

$$= \sigma^4 \sum_j \mathrm{Im}\left[\hat{a}_j e^{\mathrm{i}\hat{k}_j x}\right] \tag{A14}$$

with the complex amplitudes $\hat{a} = ae^{\mathrm{i}\phi}$ and the complex wavenumbers $\hat{k} = k + \mathrm{i}\alpha$. Using the exponential response formula, and the characteristic polynomial (A7), we obtain particular solutions of the form

$$w_{p,j} = \sigma^4 \,\mathrm{Im}\left[\frac{\hat{a}_j e^{\mathrm{i}\hat{k}_j x}}{\hat{k}_j^{\,4} + \sigma^4}\right] \tag{A15}$$

$$= \mathrm{Im}\left[\frac{\hat{a}_j e^{\mathrm{i}\hat{k}_j x}}{\left(\hat{k}_j/\sigma\right)^4 + 1}\right] \tag{A16}$$

so that the particular solution to (A1a) can be written

$$w_p = \sum_j w_{p,j}. \tag{A17}$$

In what follows, we will write

$$\tilde{a}_j = \frac{\hat{a}_j}{\left(\hat{k}_j/\sigma\right)^4 + 1} \tag{A18}$$

the complex amplitude of these solutions. As $\sigma, k_j, \alpha_j > 0$, this amplitude exists only if

$$k_j \neq \tilde{\sigma} \wedge \alpha_j \neq \tilde{\sigma}. \tag{A19}$$

A1.3 Coefficients of the homogeneous solution

The coefficients of $\boldsymbol{c}$ have to be determined to enforce the boundary conditions. Enforcing these four conditions leads to the system

$$\mathbf{D}_{\mathrm{BC}}\mathbf{M}_{\mathrm{BC}}\boldsymbol{c} = \boldsymbol{r} \tag{A20}$$

with

$$\mathbf{D}_{\mathrm{BC}} = \begin{bmatrix} 2\tilde{\sigma}^2 & 0 & 0 & 0 \\ 0 & 2\tilde{\sigma}^2 & 0 & 0 \\ 0 & 0 & 2\tilde{\sigma}^3 & 0 \\ 0 & 0 & 0 & 2\sqrt{2}\tilde{\sigma}^3 \end{bmatrix}, \tag{A21}$$

https://doi.org/10.5194/egusphere-2025-1831
Preprint. Discussion started: 3 June 2025

$$\mathbf{M}_{\mathrm{BC}} = \begin{bmatrix} 0 & 1 & 0 & -1 \\ -e^{\beta}\sin(\beta) & e^{\beta}\cos(\beta) & e^{-\beta}\sin(\beta) & -e^{-\beta}\cos(\beta) \\ -1 & 1 & 1 & 1 \\ -e^{\beta}\sin(\beta+\frac{\pi}{4}) & e^{\beta}\cos(\beta+\frac{\pi}{4}) & e^{-\beta}\cos(\beta+\frac{\pi}{4}) & e^{-\beta}\sin(\beta+\frac{\pi}{4}) \end{bmatrix}, \tag{A22}$$

where $\beta = \tilde{\sigma}L$, and

$$\boldsymbol{r} = \mathrm{Im}\sum_j \begin{bmatrix} \hat{k}_j^2\tilde{a}_j \\ \hat{k}_j{}^2\tilde{a}_j e^{\mathrm{i}\hat{k}_j L} \\ \mathrm{i}\hat{k}_j^3\tilde{a}_j \\ \mathrm{i}\hat{k}_j^3\tilde{a}_j e^{\mathrm{i}\hat{k}_j L} \end{bmatrix}. \tag{A23}$$

The third and first lines of the system give

$$\begin{cases} c_1 = \dfrac{1}{2\tilde{\sigma}^2}\left(r_1 - \dfrac{r_3}{\tilde{\sigma}}\right) + c_3 + 2c_4 & \text{(A24a)} \\ c_2 = \dfrac{r_1}{2\tilde{\sigma}^2} + c_4 & \text{(A24b)} \end{cases}$$

and the system (A20) can be simplified to the more tractable

$$\mathbf{M}_{\mathrm{II}} \begin{bmatrix} c_3 \\ c_4 \end{bmatrix} = \begin{bmatrix} -r_3 \\ r_4 \end{bmatrix} \tag{A25}$$

with

$$\mathbf{M}_{\mathrm{II}} = 2\begin{bmatrix} \sin(\beta)\sinh(\beta) & e^{\beta}\sin(\beta) - \cos(\beta)\sinh(\beta) \\ -\frac{\sqrt{2}}{2}\left[\sin(\beta)\cosh(\beta) + \cos(\beta)\sinh(\beta)\right] & -\frac{\sqrt{2}}{2}e^{\beta} - \sin(\beta+\frac{\pi}{4})\sinh(\beta) \end{bmatrix}. \tag{A26}$$

The determinant of $\mathbf{M}_{\mathrm{II}}$ is

$$\Delta = \sqrt{2}\left[2\sin^2(\beta) - \cosh(2\beta) + 1\right] \tag{A27}$$

so that $\Delta < 0$ for $\beta > 0$, and $\lim_{\beta\to 0}\Delta = 0$. Therefore, the system (A20) admits a unique solution as long as L is non-zero, and L_D finite. Solving (A25) and substituting into (A24) leads to the solution to (A20), that can be written

$$\boldsymbol{c} = \mathbf{M}\boldsymbol{r} \tag{A28}$$

https://doi.org/10.5194/egusphere-2025-1831
Preprint. Discussion started: 3 June 2025

where the coefficients of the matrix $\mathbf{M}$ are

$$M_{11} = \frac{1}{Q}e^{-2\beta}\left[\sqrt{2}\sin\left(2\beta+\frac{\pi}{4}\right) - e^{-2\beta}\right] \tag{A29a}$$

$$M_{12} = -\frac{1}{Q}e^{-\beta}\left[\sqrt{2}\cos\left(\beta+\frac{\pi}{4}\right) + e^{-2\beta}\left(3\sin\beta - \cos\beta\right)\right] \tag{A29b}$$

$$M_{13} = \frac{1}{\tilde{\sigma}Q}e^{-2\beta}\left[\sin(2\beta) - 1 + e^{-2\beta}\right] \tag{A29c}$$

$$M_{14} = \frac{1}{\tilde{\sigma}Q}e^{-\beta}\left[\cos\beta - e^{-2\beta}(2\sin\beta + \cos\beta)\right] \tag{A29d}$$

$$M_{21} = \frac{1}{Q}e^{-2\beta}\left[-\sqrt{2}\cos\left(2\beta+\frac{\pi}{4}\right) + 2 - e^{-2\beta}\right] \tag{A29e}$$

$$M_{22} = \frac{\sqrt{2}}{Q}e^{-\beta}\left[-\sin\left(\beta+\frac{\pi}{4}\right) + e^{-2\beta}\cos\left(\beta+\frac{\pi}{4}\right)\right] \tag{A29f}$$

$$M_{23} = \frac{1}{\tilde{\sigma}Q}e^{-2\beta}\left[1 - \cos(2\beta)\right] \tag{A29g}$$

$$M_{24} = \frac{1}{\tilde{\sigma}Q}e^{-\beta}\sin\beta\left[1 - e^{-2\beta}\right] \tag{A29h}$$

$$M_{31} = \frac{1}{Q}\left[-1 + \sqrt{2}e^{-2\beta}\cos\left(2\beta+\frac{\pi}{4}\right)\right] \tag{A29i}$$

$$M_{32} = \frac{1}{Q}e^{-\beta}\left[3\sin\beta + \cos\beta - \sqrt{2}e^{-2\beta}\sin\left(\beta+\frac{\pi}{4}\right)\right] \tag{A29j}$$

$$M_{33} = \frac{1}{\tilde{\sigma}Q}\left[-1 + e^{-2\beta}(\sin(2\beta)+1)\right] \tag{A29k}$$

$$M_{34} = \frac{1}{\tilde{\sigma}Q}e^{-\beta}\left[\cos\beta - 2\sin\beta - e^{-2\beta}\cos\beta\right] \tag{A29l}$$

$$M_{41} = \frac{1}{Q}\left[1 + e^{-2\beta}\left(\sqrt{2}\sin\left(2\beta+\frac{\pi}{4}\right) - 2\right)\right] \tag{A29m}$$

$$M_{42} = M_{22} \tag{A29n}$$

$$M_{43} = M_{23} \tag{A29o}$$

$$M_{44} = M_{24} \tag{A29p}$$

with

$$Q = -2\tilde{\sigma}^2\left[\left(1 - e^{-2\beta}\right)^2 + 2e^{-2\beta}\left(\cos(2\beta) - 1\right)\right]. \tag{A30}$$

The coefficients of $\mathbf{M}$ are implicit functions of $\tilde{\sigma}$, and we note that the coefficients M_{1j} are even-symmetric to the coefficients M_{3j}, and the coefficients M_{2j} are odd-symmetric to the coefficients M_{4j}. This reproduces the respective evenness and oddness of f_1 and f_3, and f_2 and f_4. The leading exponential terms for all the coefficients M_{1j} and M_{2j} ensure that the deflection does not diverge for large floes.

The homogeneous solution to (A1) is then

$$w_h(x) = \sum_j c_j f_j(x) \tag{A31}$$

https://doi.org/10.5194/egusphere-2025-1831
Preprint. Discussion started: 3 June 2025

with the coefficients of $\boldsymbol{f}$ given from (A28).

A1.4 Summary

The solution to the BVP (A1) is given by the sum

$$w(x) = w_h(x) + w_p(x) \tag{A32a}$$

$$= \sum_{j=1}^{4} c_j f_j(x) + \sum_{j=1}^{N_f} \mathrm{Im}\left[\tilde{a}_j e^{\mathrm{i}\hat{k}_j x}\right]. \tag{A32b}$$

The definitions of the functions f_j are given in Section A1.1, the definitions of the coefficients $\tilde{a}_j$ as well as the complex wavenumbers $\hat{k}_j$ are given in Section A1.2, and the definitions of the coefficients c_j in Section A1.3. The integer N_f is the number of frequency bins used to discretise a wave spectrum. The deflection is entirely determined by the elastic length L_D, the floe length L, and N_f tuples of amplitude a, wavenumber k, attenuation number α, and phase ϕ. Assuming independence of these quantities, the solution is parametrised by $2 + 4N_f$ real numbers. All of these, at the exceptions of the phases taking values in $(-\pi, \pi]$, are positive. They can be further constrained to physically realistic ranges.

A2 Elastic energy

A2.1 Introduction

The elastic energy of a bent floe is defined as

$$E = \frac{D}{2h} \int_0^L \left(\frac{\mathrm{d}^2 w}{\mathrm{d}x^2}\right)^2 \mathrm{d}x. \tag{A33}$$

We introduce the floe curvature $\kappa(x) \coloneqq \frac{\mathrm{d}^2 w}{\mathrm{d}x^2}$. From (A32), we have

$$\kappa_h = 2\tilde{\sigma}^2(-c_1 f_2 + c_2 f_1 + c_3 f_4 - c_4 f_3) \tag{A34}$$

$$\kappa_p = -\sum_j \mathrm{Im}[\hat{k}_j^2 \tilde{a}_j e^{\mathrm{i}\hat{k}x}]. \tag{A35}$$

Let us define $b_j \coloneqq |\hat{k}_j^2 \tilde{a}_j|$, $\beta_j \coloneqq \mathrm{Ang}\, \hat{k}_j^2 \tilde{a}_j$. We can then rewrite

$$\kappa_p = -\sum_j b_j e^{-\alpha_j x} \sin(k_j x + \beta_j). \tag{A36}$$

Finally, we introduce the quantities

$$E_h = \int_0^L {\kappa_h}^2 \,\mathrm{d}x, E_p = \int_0^L {\kappa_p}^2 \,\mathrm{d}x, E_q = \int_0^L \kappa_h \kappa_p \,\mathrm{d}x, \tag{A37}$$

which are the contribution to the elastic energy of respectively the homogeneous part of the displacement, the inhomogeneous part of the displacement, and their quadratic interaction.

https://doi.org/10.5194/egusphere-2025-1831
Preprint. Discussion started: 3 June 2025

A2.2 Homogeneous contribution

We start by expanding E_h as

$$E_h = {c_1}^2 I_2 + {c_2}^2 I_1 + {c_3}^2 I_4 + {c_4}^2 I_3 + 2(-c_1 c_2 I_{12} - c_1 c_3 I_{24} + c_1 c_4 I_{23} + c_2 c_3 I_{14} - c_2 c_4 I_{13} - c_3 c_4 I_{34}), \quad \text{(A38)}$$

with

$$I_j = \int_0^L {f_j}^2 \, \mathrm{d}x, I_{jn} = \int_0^L f_j f_n \, \mathrm{d}x. \quad \text{(A39)}$$

These integrals evaluate to

$$I_1 = \frac{e^{2\beta}(\sqrt{2}\sin(2\beta + \frac{\pi}{4}) + 2) - 3}{8\tilde{\sigma}} \quad \text{(A40a)}$$

$$I_2 = \frac{e^{2\beta}(-\sqrt{2}\sin(2\beta + \frac{\pi}{4}) + 2) - 1}{8\tilde{\sigma}} \quad \text{(A40b)}$$

$$I_3 = \frac{-e^{-2\beta}(\sqrt{2}\cos(2\beta + \frac{\pi}{4}) + 2) + 3}{8\tilde{\sigma}} \quad \text{(A40c)}$$

$$I_4 = \frac{e^{-2\beta}(\sqrt{2}\cos(2\beta + \frac{\pi}{4}) - 2) + 1}{8\tilde{\sigma}} \quad \text{(A40d)}$$

$$I_{12} = \frac{-\sqrt{2}e^{2\beta}\cos(2\beta + \frac{\pi}{4}) + 1}{8\tilde{\sigma}} \quad \text{(A40e)}$$

$$I_{13} = \frac{L}{2} + \frac{\sin(2\beta)}{4\tilde{\sigma}} \quad \text{(A40f)}$$

$$I_{14} = \frac{\sin^2\beta}{2\tilde{\sigma}} \quad \text{(A40g)}$$

$$I_{23} = \frac{\sin^2\beta}{2\tilde{\sigma}} \quad \text{(A40h)}$$

$$I_{24} = \frac{L}{2} - \frac{\sin(2\beta)}{4\tilde{\sigma}} \quad \text{(A40i)}$$

$$I_{34} = \frac{-\sqrt{2}e^{-2\beta}\sin(2\beta + \frac{\pi}{4}) + 1}{8\tilde{\sigma}}. \quad \text{(A40j)}$$

The products of c_j, c_n pairs simplify little, and can be evaluated numerically.

A2.3 Particular contribution

We can expand E_p as

$$E_p = \sum_{j=1}^{N_f} \left[{b_j}^2 I_j^p + 2 \sum_{n=j+1}^{N_f} b_j b_n I_{j,n} \right] \quad \text{(A41)}$$

https://doi.org/10.5194/egusphere-2025-1831
Preprint. Discussion started: 3 June 2025

with

$$I_j^p = \frac{1}{2}\int_0^L e^{-2\alpha_j x}\left[1-\cos\left(2k_j x+2\beta_j\right)\right]\mathrm{d}x \tag{A42a}$$

$$I_{j,n} = \frac{1}{2}\int_0^L e^{-\alpha_{j,n} x}\left[\cos\left(k_{j,n}^- x+\beta_{j,n}^-\right)-\cos\left(k_{j,n}^+ x+\beta_{j,n}^+\right)\right]\mathrm{d}x \tag{A42b}$$

where

$$\alpha_{j,n} \coloneqq \alpha_j+\alpha_n, k_{j,n}^{\pm} \coloneqq k_j \pm k_n, \beta_{j,n}^{\pm} \coloneqq \beta_j \pm \beta_n. \tag{A43}$$

Let us define $K_j \coloneqq |\hat{k}_j|$, $\theta_j \coloneqq \mathrm{Ang}\,\hat{k}_j$. Assuming $\alpha_j \neq 0$, we can then evaluate

$$I_j^p = \frac{1}{4}\left[\frac{1-e^{-2\alpha_j L}}{\alpha_j}+\frac{\sin(2\beta_j-\theta_j)-e^{-2\alpha_j L}\sin(2k_j L+2\beta_j-\theta_j)}{K_j}\right]. \tag{A44}$$

Similarly, we define $K_{j,n}^{\pm} \coloneqq |k_{j,n}^{\pm}+\mathrm{i}\alpha_{j,n}|$ and $\theta_{j,n}^{\pm} \coloneqq \mathrm{Ang}\,(k_{j,n}^{\pm}+\mathrm{i}\alpha_{j,n})$, which leads to

$$I_{j,n} = \frac{1}{2}\left[\frac{\sin(\beta_{j,n}^+-\theta_{j,n}^+)-e^{-\alpha_{j,n}L}\sin(k_{j,n}^+ L+\beta_{j,n}^+-\theta_{j,n}^+)}{K_{j,n}^+}\right.$$
$$\left.-\frac{\sin(\beta_{j,n}^--\theta_{j,n}^-)-e^{-\alpha_{j,n}L}\sin(k_{j,n}^- L+\beta_{j,n}^--\theta_{j,n}^-)}{K_{j,n}^-}\right]. \tag{A45}$$

A2.4 Quadratic interaction contribution

We can expand E_q as

$$E_q = \int_0^L -2\tilde{\sigma}^2(-c_1 f_2+c_2 f_1+c_3 f_4-c_4 f_3)\sum_j \mathrm{Im}[\hat{k}_j^2\tilde{a}_j e^{\mathrm{i}\hat{k}x}] \tag{A46}$$

$$= -2\tilde{\sigma}^2\sum_{j=1}^{N_f} b_j[-c_1 I_{2,j}^q+c_2 I_{1,j}^q+c_3 I_{4,j}^q-c_4 I_{3,j}^q] \tag{A47}$$

with

$$I_{n,j}^p = \int_0^L f_n(x)\exp\left(-\alpha_j x\right)\sin\left(k_j x+\beta_j\right)\mathrm{d}x. \tag{A48}$$

We define

$$Q_j^{++} = (\tilde{\sigma}+\alpha_j)^2+(\tilde{\sigma}+k_j)^2 \tag{A49a}$$

$$Q_j^{+-} = (\tilde{\sigma}+\alpha_j)^2+(\tilde{\sigma}-k_j)^2 \tag{A49b}$$

$$Q_j^{-+} = (\tilde{\sigma}-\alpha_j)^2+(\tilde{\sigma}+k_j)^2 \tag{A49c}$$

$$Q_j^{--} = (\tilde{\sigma}-\alpha_j)^2+(\tilde{\sigma}-k_j)^2, \tag{A49d}$$

https://doi.org/10.5194/egusphere-2025-1831
Preprint. Discussion started: 3 June 2025

noting Q^{--} is non-zero under the same condition (A19) that $\tilde{a}$ exists.

$$I^p_{2,j} = e^{-\beta}\Bigg\{K_j\Bigg[\sin(\theta_j-\beta_j)\left(\frac{1}{Q^{-+}}-\frac{1}{Q^{--}}\right) + e^{-\alpha_j L}\left[\frac{\sin\big((\tilde{\sigma}+k_j)L-\theta_j+\beta_j\big)}{Q^{-+}}+\frac{\sin\big((\tilde{\sigma}-k_j)L+\theta_j-\beta_j\big)}{Q^{--}}\right]\Bigg] + \sqrt{2}\tilde{\sigma}\Bigg[-\frac{\sin\big(\beta_j+\frac{\pi}{4}\big)}{Q^{-+}}-\frac{\cos\big(\beta_j+\frac{\pi}{4}\big)}{Q^{--}} + e^{-\alpha_j L}\left[\frac{\sin\big((\tilde{\sigma}+k_j)L+\beta_j+\frac{\pi}{4}\big)}{Q^{-+}}-\frac{\sin\big((\tilde{\sigma}-k_j)L-\beta_j+\frac{\pi}{4}\big)}{Q^{--}}\right]\Bigg]\Bigg\} \quad \text{(A50a)}$$

$$I^p_{1,j} = e^{-\beta}\Bigg\{K_j\Bigg[\cos(\theta_j-\beta_j)\left(\frac{1}{Q^{-+}}+\frac{1}{Q^{--}}\right) + e^{-\alpha_j L}\left[-\frac{\cos\big((\tilde{\sigma}+k_j)L-\theta_j+\beta_j\big)}{Q^{-+}}+\frac{\cos\big((\tilde{\sigma}-k_j)L+\theta_j-\beta_j\big)}{Q^{--}}\right]\Bigg] + \sqrt{2}\tilde{\sigma}\Bigg[\frac{\cos\big(\beta_j+\frac{\pi}{4}\big)}{Q^{-+}}-\frac{\sin\big(\beta_j+\frac{\pi}{4}\big)}{Q^{--}} + e^{-\alpha_j L}\left[-\frac{\cos\big((\tilde{\sigma}+k_j)L+\beta_j+\frac{\pi}{4}\big)}{Q^{-+}}+\frac{\cos\big((\tilde{\sigma}-k_j)L-\beta_j+\frac{\pi}{4}\big)}{Q^{--}}\right]\Bigg]\Bigg\} \quad \text{(A50b)}$$

$$I^p_{4,j} = e^{-\beta}\Bigg\{K_j\Bigg[-\sin(\theta_j-\beta_j)\left(\frac{1}{Q^{++}}-\frac{1}{Q^{+-}}\right) + e^{-\alpha_j L}\left[-\frac{\sin\big((\tilde{\sigma}+k_j)L-\theta_j+\beta_j\big)}{Q^{++}}+\frac{\sin\big((\tilde{\sigma}-k_j)L+\theta_j-\beta_j\big)}{Q^{+-}}\right]\Bigg] + \sqrt{2}\tilde{\sigma}\Bigg[-\frac{\cos\big(\beta_j+\frac{\pi}{4}\big)}{Q^{++}}-\frac{\sin\big(\beta_j+\frac{\pi}{4}\big)}{Q^{+-}} + e^{-\alpha_j L}\left[\frac{\cos\big((\tilde{\sigma}+k_j)L+\beta_j+\frac{\pi}{4}\big)}{Q^{++}}-\frac{\cos\big((\tilde{\sigma}-k_j)L-\beta_j+\frac{\pi}{4}\big)}{Q^{+-}}\right]\Bigg]\Bigg\} \quad \text{(A50c)}$$

$$I^p_{3,j} = e^{-\beta}\Bigg\{K_j\Bigg[-\cos(\theta_j-\beta_j)\left(\frac{1}{Q^{++}}-\frac{1}{Q^{+-}}\right) + e^{-\alpha_j L}\left[\frac{\cos\big((\tilde{\sigma}+k_j)L-\theta_j+\beta_j\big)}{Q^{++}}+\frac{\cos\big((\tilde{\sigma}-k_j)L+\theta_j-\beta_j\big)}{Q^{+-}}\right]\Bigg] + \sqrt{2}\tilde{\sigma}\Bigg[-\frac{\sin\big(\beta_j+\frac{\pi}{4}\big)}{Q^{++}}-\frac{\cos\big(\beta_j+\frac{\pi}{4}\big)}{Q^{+-}} + e^{-\alpha_j L}\left[\frac{\sin\big((\tilde{\sigma}+k_j)L+\beta_j+\frac{\pi}{4}\big)}{Q^{++}}-\frac{\sin\big((\tilde{\sigma}-k_j)L-\beta_j+\frac{\pi}{4}\big)}{Q^{+-}}\right]\Bigg]\Bigg\}. \quad \text{(A50d)}$$

https://doi.org/10.5194/egusphere-2025-1831
Preprint. Discussion started: 3 June 2025

Author contributions. NM developed the model off an initial version developed by JPA and AT, designed the numerical experiments, and conducted the analysis, with input from the other authors. NM and VD led the writing with suggestions and improvements from GB. VD supervised the study.

Competing interests. The authors have no competing interests.

Acknowledgements. The authors thank Baptiste Auvity, Stéphane Perrard, Antonin Eddi, Dany Dumont, and Vasco Zanchi for fruitful discussions which have significantly improved the quality of this manuscript.

Financial support. This research received support through Schmidt Sciences, LLC, via the SASIP project (grant G-24-66154).

https://doi.org/10.5194/egusphere-2025-1831
Preprint. Discussion started: 3 June 2025

References

Ardhuin, F., Otero, M., Merrifield, S., Grouazel, A., and Terrill, E.: Ice breakup controls dissipation of wind waves across Southern Ocean Sea Ice, Geophysical Research Letters, 47, e2020GL087 699, 2020.

Asplin, M. G., Galley, R., Barber, D. G., and Prinsenberg, S.: Fracture of summer perennial sea ice by ocean swell as a result of Arctic storms, Journal of Geophysical Research: Oceans, 117, https://doi.org/https://doi.org/10.1029/2011JC007221, 2012.

Auclair, J.-P., Dumont, D., Lemieux, J.-F., and Ritchie, H.: A model study of convergent dynamics in the marginal ice zone, Philosophical Transactions of the Royal Society A, 380, 20210 261, 2022.

Auvity, B., Duchemin, L., Eddi, A., and Perrard, S.: Wave induced fracture of a sea ice analog, https://doi.org/10.48550/ARXIV.2501.04824, 2025.

Balasoiu, D.: Modélisation et simulation du comportement mécanique de floes de glace, Ph.D. thesis, Université Grenoble Alpes, 2020.

Bateson, A. W., Feltham, D. L., Schröder, D., Hosekova, L., Ridley, J. K., and Aksenov, Y.: Impact of sea ice floe size distribution on seasonal fragmentation and melt of Arctic sea ice, The Cryosphere, 14, 403–428, https://doi.org/10.5194/tc-14-403-2020, publisher: Copernicus GmbH, 2020.

Blanchard-Wrigglesworth, E., Donohoe, A., Roach, L. A., DuVivier, A., and Bitz, C. M.: High-Frequency Sea Ice Variability in Observations and Models, Geophysical Research Letters, 48, e2020GL092 356, https://doi.org/https://doi.org/10.1029/2020GL092356, 2021.

Blanchard-Wrigglesworth, E., Webster, M., Boisvert, L., Parker, C., and Horvat, C.: Record Arctic Cyclone of January 2022: Characteristics, Impacts, and Predictability, Journal of Geophysical Research: Atmospheres, 127, e2022JD037 161, https://doi.org/https://doi.org/10.1029/2022JD037161, e2022JD037161 2022JD037161, 2022.

Collins, C. O., Rogers, W. E., Marchenko, A., and Babanin, A. V.: In situ measurements of an energetic wave event in the Arctic marginal ice zone: Largest Waves Measured in Arctic Ice, Geophysical Research Letters, 42, 1863–1870, https://doi.org/10.1002/2015GL063063, 2015.

Dempsey, J. P.: The Fracture Toughness of Ice, in: Ice-Structure Interaction, edited by Jones, S., Tillotson, J., McKenna, R. F., and Jordaan, I. J., pp. 109–145, Springer Berlin Heidelberg, Berlin, Heidelberg, 1991.

Dolatshah, A., Nelli, F., Bennetts, L. G., Alberello, A., Meylan, M. H., Monty, J. P., and Toffoli, A.: Letter: Hydroelastic interactions between water waves and floating freshwater ice, Physics of Fluids, 30, 091 702, https://doi.org/10.1063/1.5050262, 2018.

Dumas-Lefebvre, E. and Dumont, D.: Aerial observations of sea ice breakup by ship waves, The Cryosphere, 17, 827–842, https://doi.org/10.5194/tc-17-827-2023, 2023.

Dumont, D.: Marginal ice zone dynamics: history, definitions and research perspectives, Philosophical Transactions of the Royal Society A, 380, 20210 253, https://doi.org/https://doi.org/10.1098/rsta.2021.0253, 2022.

Dumont, D., Kohout, A., and Bertino, L.: A wave-based model for the marginal ice zone including a floe breaking parameterization, Journal of Geophysical Research: Oceans, 116, 2011.

Fox, C. and Squire, V. A.: Strain in shore fast ice due to incoming ocean waves and swell, Journal of Geophysical Research: Oceans, 96, 4531–4547, https://doi.org/https://doi.org/10.1029/90JC02270, 1991.

Francfort, G.: Variational fracture: twenty years after, International Journal of Fracture, pp. 1–11, 2021.

Francfort, G. and Marigo, J.-J.: Revisiting brittle fracture as an energy minimization problem, Journal of the Mechanics and Physics of Solids, 46, 1319–1342, https://doi.org/https://doi.org/10.1016/S0022-5096(98)00034-9, 1998.

https://doi.org/10.5194/egusphere-2025-1831
Preprint. Discussion started: 3 June 2025

Gharamti, I., Dempsey, J., Polojärvi, A., and Tuhkuri, J.: Fracture energy of columnar freshwater ice: Influence of loading type, loading rate and size, Materialia, 20, 101 188, https://doi.org/https://doi.org/10.1016/j.mtla.2021.101188, 2021a.

Gharamti, I. E., Dempsey, J. P., Polojärvi, A., and Tuhkuri, J.: Creep and fracture of warm columnar freshwater ice, The Cryosphere, 15, 2401–2413, https://doi.org/10.5194/tc-15-2401-2021, 2021b.

Griffith, A. A.: The phenomena of rupture and flow in solids, Philosophical transactions of the royal society of london. Series A, containing papers of a mathematical or physical character, 221, 163–198, 1921.

He, K., Ni, B., Xu, X., Wei, H., and Xue, Y.: Numerical simulation on the breakup of an ice sheet induced by regular incident waves, Applied Ocean Research, 120, 103 024, https://doi.org/https://doi.org/10.1016/j.apor.2021.103024, 2022.

Herman, A.: Wave-induced stress and breaking of sea ice in a coupled hydrodynamic discrete-element wave–ice model, The Cryosphere, 11, 2711–2725, 2017.

Herman, A.: Wave-Induced Surge Motion and Collisions of Sea Ice Floes: Finite-Floe-Size Effects, Journal of Geophysical Research: Oceans, 123, 7472–7494, 2018.

Horvat, C.: Floes, the marginal ice zone and coupled wave-sea-ice feedbacks, Philosophical Transactions of the Royal Society A, 380, 20210 252, 2022.

Horvat, C. and Tziperman, E.: A prognostic model of the sea-ice floe size and thickness distribution, The Cryosphere, 9, 2119–2134, https://doi.org/10.5194/tc-9-2119-2015, 2015.

Kohout, A. and Meylan, M.: An elastic plate model for wave attenuation and ice floe breaking in the marginal ice zone, Journal of Geophysical Research: Oceans, 113, 2008.

Kohout, A., Williams, M., Toyota, T., Lieser, J., and Hutchings, J.: In situ observations of wave-induced sea ice breakup, Deep Sea Research Part II: Topical Studies in Oceanography, 131, 22–27, https://doi.org/10.1016/j.dsr2.2015.06.010, 2016.

Meylan, M., Bennetts, L., Cavaliere, C., Alberello, A., and Toffoli, A.: Experimental and theoretical models of wave-induced flexure of a sea ice floe, Physics of Fluids, 27, 041 704, 2015.

Mokus, N. G. A.: sasip-climate/ff1d-ftsw-pub: ff1d-ftsw-pub v1.0.1, https://doi.org/10.5281/zenodo.15230102, 2025a.

Mokus, N. G. A.: sasip-climate/ff1d-ftsw-pub-ice: v1.0.0, https://doi.org/10.5281/zenodo.15528650, 2025b.

Mokus, N. G. A.: sasip-climate/swiift: v0.7.0, https://doi.org/10.5281/zenodo.15528673, 2025c.

Mokus, N. G. A. and Montiel, F.: Wave-triggered breakup in the marginal ice zone generates lognormal floe size distributions: a simulation study, The Cryosphere, 16, 4447–4472, https://doi.org/10.5194/tc-16-4447-2022, 2022.

Montiel, F. and Squire, V. A.: Modelling wave-induced sea ice break-up in the marginal ice zone, Proceedings of the Royal Society A: Mathematical, Physical and Engineering Sciences, 473, 20170 258, https://doi.org/http://dx.doi.org/10.1098/rspa.2017.0258, 2017.

Moreau, L., Boué, P., Serripierri, A., Weiss, J., Hollis, D., Pondaven, I., Vial, B., Garambois, S., Larose, É., Helmstetter, A., Stehly, L., Hillers, G., and Gilbert, O.: Sea Ice Thickness and Elastic Properties From the Analysis of Multimodal Guided Wave Propagation Measured With a Passive Seismic Array, Journal of Geophysical Research: Oceans, 125, e2019JC015 709, https://doi.org/https://doi.org/10.1029/2019JC015709, 2020a.

Moreau, L., Weiss, J., and Marsan, D.: Accurate Estimations of Sea-Ice Thickness and Elastic Properties From Seismic Noise Recorded With a Minimal Number of Geophones: From Thin Landfast Ice to Thick Pack Ice, Journal of Geophysical Research: Oceans, 125, https://doi.org/10.1029/2020jc016492, 2020b.

Mulmule, S. and Dempsey, J. P.: A viscoelastic fictitious crack model for the fracture of sea ice, Mechanics of Time-Dependent Materials, 1, 331–356, 1997.

https://doi.org/10.5194/egusphere-2025-1831
Preprint. Discussion started: 3 June 2025

Passerotti, G., Bennetts, L. G., von Bock und Polach, F., Alberello, A., Puolakka, O., Dolatshah, A., Monbaliu, J., and Toffoli, A.: Interactions between irregular wave fields and sea ice: A physical model for wave attenuation and ice breakup in an ice tank, Journal of Physical Oceanography, 52, 1431–1446, 2022.

Raphael, M. N., Maierhofer, T. J., Fogt, R. L., Hobbs, W. R., and Handcock, M. S.: A twenty-first century structural change in Antarctica's sea ice system, Communications Earth & Environment, 6, https://doi.org/10.1038/s43247-025-02107-5, 2025.

Ren, H., Zhang, C., and Zhao, X.: Numerical simulations on the fracture of a sea ice floe induced by waves, Applied Ocean Research, 108, 102 527, https://doi.org/https://doi.org/10.1016/j.apor.2021.102527, 2021.

Roach, L. A., Bitz, C. M., Horvat, C., and Dean, S. M.: Advances in modeling interactions between sea ice and ocean surface waves, Journal of Advances in Modeling Earth Systems, 11, 4167–4181, https://doi.org/https://doi.org/10.1029/2019MS001836, 2019.

Smith, M., Stammerjohn, S., Persson, O., Rainville, L., Liu, G., Perrie, W., Robertson, R., Jackson, J., and Thomson, J.: Episodic Reversal of Autumn Ice Advance Caused by Release of Ocean Heat in the Beaufort Sea, Journal of Geophysical Research: Oceans, 123, 3164–3185, https://doi.org/10.1002/2018JC013764, 2018.

Squire, V. A.: Ocean Wave Interactions with Sea Ice: A Reappraisal, Annual Review of Fluid Mechanics, 52, 37–60, https://doi.org/https://doi.org/10.1146/annurev-fluid-010719-060301, 2020.

Stroeve, J. and Notz, D.: Changing state of Arctic sea ice across all seasons, Environmental Research Letters, 13, 103 001, https://doi.org/10.1088/1748-9326/aade56, 2018.

Stroeve, J. C., Serreze, M. C., Holland, M. M., Kay, J. E., Malanik, J., and Barrett, A. P.: The Arctic's rapidly shrinking sea ice cover: a research synthesis, Climatic change, 110, 1005, 2012.

Sutherland, G., Rabault, J., Christensen, K. H., and Jensen, A.: A two layer model for wave dissipation in sea ice, Applied Ocean Research, 88, 111–118, https://doi.org/https://doi.org/10.1016/j.apor.2019.03.023, 2019.

Sutherland, P. and Dumont, D.: Marginal ice zone thickness and extent due to wave radiation stress, Journal of Physical Oceanography, 48, 1885–1901, 2018.

Thomson, J.: Wave propagation in the marginal ice zone: connections and feedback mechanisms within the air–ice–ocean system, Philosophical Transactions of the Royal Society A, 380, 20210 251, https://doi.org/https://doi.org/10.1098/rsta.2021.0251, 2022.

Thomson, J. and Rogers, W. E.: Swell and sea in the emerging Arctic Ocean, Geophysical Research Letters, 41, 3136–3140, https://doi.org/10.1002/2014GL059983, 2014.

Tkacheva, L.: Scattering of surface waves by the edge of a floating elastic plate, Journal of Applied Mechanics and Technical Physics, 42, 638–646, 2001.

Virtanen, P., Gommers, R., Oliphant, T. E., Haberland, M., Reddy, T., Cournapeau, D., Burovski, E., Peterson, P., Weckesser, W., Bright, J., van der Walt, S. J., Brett, M., Wilson, J., Millman, K. J., Mayorov, N., Nelson, A. R. J., Jones, E., Kern, R., Larson, E., Carey, C. J., Polat, İ., Feng, Y., Moore, E. W., VanderPlas, J., Laxalde, D., Perktold, J., Cimrman, R., Henriksen, I., Quintero, E. A., Harris, C. R., Archibald, A. M., Ribeiro, A. H., Pedregosa, F., van Mulbregt, P., and SciPy 1.0 Contributors: SciPy 1.0: Fundamental Algorithms for Scientific Computing in Python, Nature Methods, 17, 261–272, https://doi.org/10.1038/s41592-019-0686-2, 2020.

Voermans, J. J., Rabault, J., Filchuk, K., Ryzhov, I., Heil, P., Marchenko, A., Collins III, C. O., Dabboor, M., Sutherland, G., and Babanin, A. V.: Experimental evidence for a universal threshold characterizing wave-induced sea ice break-up, The Cryosphere, 14, 4265–4278, https://doi.org/https://doi.org/10.5194/tc-14-4265-2020, 2020.

Williams, T. D., Rampal, P., and Bouillon, S.: Wave-ice interactions in the neXtSIM sea ice model, The Cryosphere Discussions, https://doi.org/10.5194/tc-2017-24, 2017.

https://doi.org/10.5194/egusphere-2025-1831
Preprint. Discussion started: 3 June 2025

Yang, C.-Y., Liu, J., and Chen, D.: Understanding the influence of ocean waves on Arctic sea ice simulation: a modeling study with an atmosphere–ocean—wave-–sea ice coupled model, The Cryosphere, 18, 1215–1239, https://doi.org/10.5194/tc-18-1215-2024, 2024.

Zhang, C. and Zhao, X.: Theoretical model for predicting the break-up of ice covers due to wave–ice interaction, Applied Ocean Research, 112, 102 614, https://doi.org/10.1016/j.apor.2021.102614, 2021.